Data-Centric Engineering (2026), 7: e18
doi:10.1017/dce.2026.10051

CAMBRIDGE UNIVERSITY PRESS

RESEARCH ARTICLE

Nonlinear system identification for model-based control of waked wind turbines

Sebastiano Randino[1,2], Lorenzo Schena[1,3], Nicolas Coudou[1], Emanuele Garone[2] and Miguel Alfonso Mendez[1,4,5]

[1]Environmental and Applied Fluid Dynamics Department, von Karman Institute For Fluid Dynamics, Rhode-St-Genèse, Belgium
[2]Service d'Automatique et d'Analyse des Systèmes, Université libre de Bruxelles (ULB), Brussels, Belgium
[3]Department of Mechanical Engineering, Vrije Universiteit Brussel (VUB), Brussels, Belgium
[4]Aerospace Engineering Research Group, Universidad Carlos III de Madrid, Leganés, Spain
[5]Aero-Thermo-Mechanics Laboratory, Université libre de Bruxelles (ULB), Brussels, Belgium
Corresponding author: Sebastiano Randino; Email: sebastiano.randino@vki.ac.be

Received: 15 October 2025; **Revised:** 23 March 2026; **Accepted:** 09 April 2026

Keywords: adjoint-based optimization; data-driven control strategies; nonlinear system identification; online model adaptation; surrogate aerodynamic models

Abstract

This work presents a nonlinear system identification framework for modeling the power extraction dynamics of wind turbines, including both freestream and waked conditions. The approach models turbine dynamics using data-driven power coefficient maps expressed as combinations of compact radial basis functions and polynomial bases, parameterized in terms of tip-speed ratio and upstream conditions. These surrogate models are embedded in a first-order dynamic system suitable for model-based control. Experimental validation is carried out in two wind tunnel configurations: a low-turbulence tandem setup and a high-turbulence wind farm scenario. In the tandem case, the identified model is integrated into an adapted $K\omega^2$ controller, resulting in improved tip-speed ratio tracking and power stability compared to steady-state models, while also outperforming the BEM-based model in the present low Reynolds number setting, where aerodynamic predictions are more uncertain. In the wind farm scenario, the model captures the statistical behavior of the turbines despite unresolved turbulence. The proposed method enables interpretable, adaptive control across a range of operating conditions without relying on black-box learning strategies.

Impact statement

This study introduces a nonlinear system identification framework for wind turbines that bridges the gap between physics-based models and data-driven learning. By embedding interpretable surrogate aerodynamic models into control-oriented formulations, the method enables online adaptation to both freestream and waked conditions. The framework is experimentally validated and shown to enhance control performance compared to steady-state approaches and a BEM-based model in the present low Reynolds number setting. These findings advance the reliability of model-based wind turbine control and open perspectives for adaptive, data-centric strategies in wind farm operation, with potential to improve energy yield and resilience. In practice, this could support full-scale deployment through periodic model adaptation and integration into farm-level supervisory control systems.

This research article was awarded Open Data badge for transparent practices. See the Data Availability Statement for details.

© The Author(s), 2026. Published by Cambridge University Press. This is an Open Access article, distributed under the terms of the Creative Commons Attribution licence (http://creativecommons.org/licenses/by/4.0), which permits unrestricted re-use, distribution and reproduction, provided the original article is properly cited.

https://doi.org/10.1017/dce.2026.10051 Published online by Cambridge University Press

1. Introduction

Wind energy is the fastest-growing renewable sector and a cornerstone of global decarbonization efforts. In Europe, the installed capacity has doubled from 128 GW in 2014 to 255 GW today (WindEurope, 2015, 2025). To meet rising demand, turbines have grown over tenfold in size and are increasingly clustered into large wind farms (Caduff et al., 2012; Porté-Agel et al., 2020). As wind speed varies, wind turbines are controlled to maximize energy capture at low wind speeds, while constraining power output and mitigating structural loads at high wind speeds (Wright and Fingersh, 2008).

Control of wind turbines has received enormous attention in recent years, with research increasingly focusing on advanced strategies. Approaches such as fuzzy logic control (FLC, Bharani and Sivaprakasam, 2022; Borunda et al., 2024; Maafa et al., 2024), sliding mode control (SMC Echiheb et al., 2022; Zribi et al., 2017), maximum power point tracking (MPPT Abdullah et al., 2012; Pande and Nasikkar, 2023), and model predictive control (MPC Schlipf et al., 2013; Silva et al., 2022)—have been proposed to enhance robustness and adaptability under varying conditions. However, their adoption remains limited due to practical challenges such as the need for expert tuning (FLC), high-frequency oscillations (SMC), sensitivity to wind fluctuations (MPPT), and computational demands (MPC). In recent years, AI-driven control approaches have emerged as a compelling alternative, leveraging data to design or adapt controllers capable of handling nonlinear, poorly modeled turbine dynamics (Tomin et al., 2019; Sierra-García and Santos, 2020). Methods based on artificial neural networks (ANN, Majout et al., 2024), adaptive neuro-fuzzy inference systems (ANFIS, Chhipa et al., 2021), reinforcement learning (RL, Schena et al., 2022; Soler et al., 2024), and evolutionary algorithms (GA, Guediri et al., 2023, PSO Khurshid et al., 2022) have demonstrated promising performance in simulations. Nonetheless, their application in operational turbines remains constrained by stringent industry requirements for reliability, consistency, and certifiability (Chatterjee and Dethlefs, 2021). Emerging directions such as safe reinforcement learning (Gu et al., 2024) seek to address these barriers, although real-world deployment is still in its early stages.

Despite the growing interest in advanced controllers, classical model-based strategies remain the standard in industrial wind turbines due to their robustness and simplicity (Wright and Fingersh, 2008; Pao and Johnson, 2009). Power maximization is traditionally carried out with torque controllers following the so-called $K\omega^2$ law, which adjusts the generator torque while maintaining a fixed, optimal blade pitch, whereas load mitigation is typically assigned to a proportional-integral (PI) controller of the blade pitch to sustain rated power output (Laks et al., 2009). These typically rely on first-order nonlinear models, whose accuracy critically impacts performance. For example, the gain K in the $K\omega^2$ controller depends on the optimal tip-speed ratio (Pao and Johnson, 2009), while PI controllers are tuned using linearized turbine dynamics (Abbas et al., 2021). A persistent challenge is the identification of the rotor's nonlinear aerodynamic behavior (Ribeiro et al., 2023). Common approaches include generating aerodynamic maps via momentum theory—most notably the blade element momentum (BEM) method—or using predefined functional forms (e.g., polynomials or sinusoids) calibrated from experimental data (Pao and Johnson, 2009; Castillo et al., 2023). Accurate aerodynamic modeling is critical for minimizing energy losses in wind turbine control, with errors potentially reducing large-scale production by up to 3% (Pao and Johnson, 2009). Moreover, model accuracy degrades over time due to structural aging, blade erosion, and ice formation (Staffell and Green, 2014; Campobasso et al., 2023). The continuous growth of turbine size and increasing wake interactions in large wind farms further challenge models originally designed for isolated turbines in steady inflow (Pao and Johnson, 2009; Shapiro et al., 2021): unsteady wake-induced conditions violate key assumptions of methods like BEM (Leishman, 2002), while blade flexibility alters aerodynamic load distributions beyond what standard models capture (Cao et al., 2022). Though dynamic BEM introduces empirical corrections (Papi et al., 2023), persistent discrepancies with real-world behavior continue to motivate research into adaptive control and system identification (Pusch et al., 2024).

To address the limitations of first-principles models under real-world conditions, system identification techniques are increasingly employed in wind turbine control (Bossanyi et al., 2012; Nelles, 2020). These data-driven approaches replace detailed physical modeling with parameter estimation from operational

https://doi.org/10.1017/dce.2026.10051 Published online by Cambridge University Press

data (Rai et al., 2017). Most methods adopt linear state-space representations around specific operating points (Houtzager et al., 2010). Examples include linear time-periodic (LTP) models identified via harmonic transfer functions using HAWC2 simulations (Allen et al., 2011), and linear time-invariant (LTI) models estimated through predictor-based subspace identification (PBSID) (Houtzager et al., 2010) or frequency domain decomposition of field data (Jasniewicz and Geyler, 2011). Simple auto-regressive (AR) models have also shown competitive accuracy with minimal parameters (Mahmoud and Qureshi, 2012). These linear models frequently support advanced control schemes such as model predictive control (MPC) (Verwaal et al., 2015). Other strategies include adaptive second-order transfer functions (Simani and Castaldi, 2013) and switching between LTI models across operating regions, with fuzzy logic used to smooth transitions (Jelavic et al., 2006).

The limitations of linear control strategies under switching conditions are discussed in Gros and Schild, 2017. Nonlinear models have demonstrated improved performance over traditional gain-scheduled PI controllers (Kumar and Stol, 2010), motivating system identification efforts using techniques such as variable-order fractional neural networks (Aslipour and Yazdizadeh, 2019), fuzzy systems (Simani, 2012), and neural networks (Kelouwani and Agbossou, 2004). Clustering-based piecewise affine models have also been explored for power regulation (Sindareh Esfahani and Pieper, 2021). However, concerns over generalization and reliability of these black-box methods have motivated hybrid methods that embed physical insights into data-driven models, improving robustness across operating conditions (Gebel et al., 2025).

A promising direction is the identification of physically interpretable quantities like power or thrust coefficients. Common approaches use polynomial models with recursive least squares (RLS) for real-time updates (Monroy and Alvarez-Icaza, 2006; Hosseinpour et al., 2017), reduced multivariate polynomial models (Son et al., 2009), or observer-based methods for dynamic estimation (Yap et al., 2012). Adaptive systems such as adaptive neuro-fuzzy inference systems (ANFIS) have also been applied to optimize power coefficient estimation and enhance performance (Petković et al., 2013; Asghar and Liu, 2017). Most adaptive modeling efforts for estimating the power coefficient have focused on isolated turbines and relied on numerical simulations where the true coefficient is known (Monroy and Alvarez-Icaza, 2006; Petković et al., 2013; Hosseinpour et al., 2017). To the authors' knowledge, no studies have retrieved experimentally the power coefficient in the presence of turbine wakes, where conventional models typically fall back on simplified, low-fidelity wake descriptions (Bhatt et al., 2022). A notable exception is Annoni et al. (2015), who identified a two-turbine array offline using linear transfer functions from experimental data. However, online assimilation of the power coefficient in multi-turbine setups remains unaddressed.

This study addresses this gap by proposing an online experimental assimilation of the power coefficient for wind turbine arrays operating under wake interactions. The approach identifies a nonlinear, first-order dynamic model of the wind turbine array configuration, suitable for model-based control applications. As a demonstrative application, we consider a small-scale set-up of two 0.15 m diameter turbines, challenging the model to also recover low Reynolds number effects, and integrate the identified model into an adapted version of the $K\omega^2$ controller. Although demonstrated here on a small-scale experimental setup, the same identification logic is compatible with full-scale turbines, where operational SCADA data and inflow sensing could be used to update control-oriented surrogate models over time.

This article is organized as follows. First, the system identification problem of a wind turbine is reviewed in Section 2 while Section 3 introduces the proposed data-driven closure laws with the identification strategy. Section 4 describes the experimental setup. Section 5 presents the results while Section 6 closes with conclusions and perspectives.

2. System identification framework

The configuration of interest is illustrated in Figure 1. It consists of identical turbines with radius R, aligned with the incoming flow and spaced at a distance L, rotating at angular velocities ω_i, subjected to an incoming flow u_i, and experiencing aerodynamic torques $\tau_{\text{aero},i}$. The subscript 1 denotes the first turbine

https://doi.org/10.1017/dce.2026.10051 Published online by Cambridge University Press

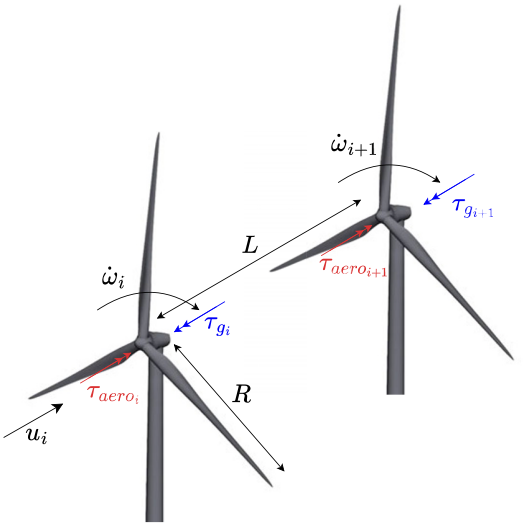


Figure 1. *Configuration of two aligned wind turbines and main variables. The downstream turbine, indexed by $i+1$, operates in the wake of the upstream turbine i, with inter-turbine spacing L, rotor radius R, inflow velocity u_i, aerodynamic torques $\tau_{\text{aero},i}$ and $\tau_{\text{aero},i+1}$, and generator torques $\tau_{g,i}$ and $\tau_{g,i+1}$.*

exposed to the freestream wind. For a generic turbine i, the subscripts i and $i+1$ refer to two consecutive turbines in the array, with turbine $i+1$ operating in the wake of turbine i. We assume that the turbines operate under a power maximization objective in the torque-controlled region; therefore, the only relevant control inputs are the generator torques $\tau_{g,i}$.

The aerodynamic torque generated by the turbines is related to the power coefficient $C_{p,i}$, defined as

$$C_{p,i} = \frac{\tau_{\text{aero},i}\,\omega_i}{\frac{1}{2}\rho\pi R^2 u_1^3}, \tag{2.1}$$

where $\tau_{\text{aero},i}\,\omega_i$ represents the aerodynamic power extracted by turbine i. In this work, $C_{p,i}$ is defined with respect to the freestream wind speed u_1, so as to provide a consistent performance metric across the array. This differs from the local definition of the power coefficient, which would instead be based on the rotor-effective velocity experienced by each turbine, denoted here by u_i.

The resulting nonlinear ODE model for a generic turbine i reads

$$\begin{cases} \dot{\omega}_i = f\left(\omega_i, u_1, \tau_{g,i}; C_{p,i}\right) \\ \omega_i(0) = \omega_{i,0} \end{cases} \tag{2.2}$$

where the dot denotes time derivatives. The function f reads

$$f\left(\omega_i, u_1, \tau_{g,i}; C_{p,i}\right) = \frac{1}{J}\left(\tau_{\text{aero},i} - \tau_{g,i}\right) = \frac{1}{J}\left(\frac{1}{2}\rho\pi R^2 \frac{C_{p,i}}{\omega_i} u_1^3 - \tau_{g,i}\right), \tag{2.3}$$

where J is the rotor moment of inertia [kg·m^2] and ρ is the air density [kg·m^{-3}]. The model considers the torque balance at the rotor level, without explicitly representing drivetrain dynamics.

The nonlinear system identification problem addressed in this work consists of modeling the power coefficients $C_{p,i}$ in Equation (2.2) as general parametric functions $\tilde{g}_i(\cdot;\mathbf{w}_i)$, where the parameters $\mathbf{w}_i \in \mathbb{R}^{n_q}$ act as closure variables. The power coefficient, therefore, plays the role of a closure term linking the aerodynamic power extraction to the rotor dynamics. The adopted closure laws distinguish between the upstream turbine and the downstream ones, and read

https://doi.org/10.1017/dce.2026.10051 Published online by Cambridge University Press

$$\begin{cases} C_{p,1} = \tilde{g}_1(\lambda_1, \mathrm{Re}; \mathbf{w}_1), \\ C_{p,i} = \tilde{g}_i(\lambda_i, \lambda_{i-1}(t-\Delta t); \mathbf{w}_i), i > 1, \end{cases} \tag{2.4}$$

where $\lambda_i = \omega_i R/u_1$ is the tip-speed ratio, $\Delta t = L/u_1$ denotes the estimated wake convection time, $\mathrm{Re} = u_1 D/\nu$ is the Reynolds number, and ν is the air kinematic viscosity. In the present formulation, both the tip-speed ratio and the Reynolds number are defined using the freestream velocity u_1.

For a given geometry and fixed blade pitch angle, the power coefficient is commonly represented as a function of the tip-speed ratio λ_i, which motivates its inclusion in both upstream and downstream models. For the upstream turbine ($i = 1$), although full-scale machines are largely insensitive to Reynolds number variations at high Reynolds numbers (Saint-Drenan et al., 2020), this dependence is retained here due to the small scale of the experimental setup (Bastankhah and Porté-Agel, 2017). For downstream turbines, wake effects are incorporated through a closure in which the influence of the upstream turbine is parameterized by its delayed tip-speed ratio $\lambda_{i-1}(t-\Delta t)$. This provides a compact, measurable, and control-relevant descriptor of the upstream operating condition, while avoiding the explicit introduction of local flow variables that are not directly accessible in the present experiments.

This formulation is a simplified model of wake interactions, as it does not resolve spatial wake structure, partial overlap, yaw misalignment, or atmospheric shear. It is therefore mainly intended for aligned configurations and controlled inflow, where the downstream turbine response is dominated by the upstream operating state. Nevertheless, the general adjoint-based online adaptation framework is more general and can be extended with additional variables when more detailed flow information and more general dynamic wake models are available.

Denoting by $\mathbf{w} = [\mathbf{w}_1, \mathbf{w}_2, \ldots] \in \mathbb{R}^{n_q}$ the concatenated parameter vector of all turbines, the identification is performed by minimizing the discrepancy between observed data and model predictions. Following a variational approach (PA; Schena et al., 2023; Marques et al., 2024), the optimal parameters minimize the cost functional

$$J_{w,i}(\mathbf{w}_i) = \frac{1}{T_0} \int_0^{T_0} L_p\big(\omega_i(t; \mathbf{w}_i), \omega_i^*(t)\big)\, dt, \tag{2.5}$$

where L_p quantifies the mismatch between the simulated state $\omega_i(t; \mathbf{w}_i)$ and the measured rotor speed $\omega_i^*(t)$. The time interval T_0 represents the observation window (episode). In the proposed framework, data are acquired in real time during each episode, whereas parameter updates are performed only at the end of the episode by solving the batch optimization problem in Equation (2.5). The method should therefore be interpreted as an episodic online adaptation strategy. As detailed in the following section, the identification is carried out independently for each turbine.

3. Power coefficient closure laws

For the first turbine ($i = 1$), the power coefficient is modeled as

$$C_{p,1}(\lambda_1, \mathrm{Re}) = \sum_{m=1}^{M} \sum_{n=1}^{N} w_{1,m,n} \phi_m\big(\lambda_1; \lambda_m^*, c_m\big)\, \psi_n(\mathrm{Re}), \tag{3.1}$$

whereas for the downstream turbines ($i > 1$), it is modeled as

$$C_{p,i}(\lambda_i, \lambda_{i-1}) = \sum_{m=1}^{M} \sum_{n=1}^{N} w_{i,m,n} \phi_m\big(\lambda_i; \lambda_m^*, c_m\big)\, \psi_n(\lambda_{i-1}). \tag{3.2}$$

where, consistently with Section 2, the upstream tip-speed ratio is evaluated at a delayed time, i.e., $\lambda_{i-1} = \lambda_{i-1}(t-\Delta t)$. The coefficients $w_{i,m,n}$ are collected in the vector $\mathbf{w}_i$ for each turbine. The functions ϕ_m and ψ_n denote radial basis functions (RBFs) and polynomial basis functions, respectively, as described in detail below. The integers M and N represent the total number of basis functions used. As

https://doi.org/10.1017/dce.2026.10051 Published online by Cambridge University Press

demonstrated in the following, the proposed formulation allows for representing a realistic nonlinear power coefficient curve while maintaining a linear dependency on the model parameters.

The functions $\phi_m\left(\lambda;\lambda_m^*,c_m\right)$ and $\psi_n(x)$ act as basis functions. The first is a basis of compact support radial basis functions (RBFs)

$$\phi_m\left(\lambda;\lambda_m^*,c_m\right)=\begin{cases}\left(1-\frac{d_m^2(\lambda)}{c_m^2}\right)^5 & \text{if}|d_m|\le c_m\\ 0 & \text{otherwise}\end{cases} \tag{3.3}$$

where $d_m(\lambda)=\lambda-\lambda_m^*$ is the distance from the RBF center λ_m^*, and c_m is the basis radius. Five of these bases are collocated in the range of admissible tip-speed ratios at centers $\lambda_m^*=[4,5,6,7,8]$, all having the same shape factor $c_m=1.5$. The number of RBFs was chosen as a compromise between ensuring sufficient flexibility to represent the useful portion of the power coefficient curve and avoiding an unnecessarily large number of basis functions. A polynomial basis up to order 2 is chosen, hence $\psi_n(x)=x^n$ with $n=[0,1,2]$. This choice was found sufficient to capture the observed dependence on the second variable while preserving a parsimonious parametrization. A more systematic sensitivity study on the number of basis functions could be considered in future works.

3.1. Initial guess for model parameters

An estimate of the coefficients $w_{i,m,n}$ can be computed using a standard least squares approach under the assumption of steady-state operation, i.e., $\dot{\omega}_i=0$. Under this condition, Equation (2.3) yields $\tau_{a,i}=\tau_{g,i}$. Substituting this relation into Equation (2.1), one obtains

$$C_{p,i}=\frac{2\tau_{g,i}\omega_i}{\rho\pi R^2u_1^3}. \tag{3.4}$$

Assuming that $\tau_{g,i}$, ω_i and u_1 are measured, Equation (3.4) can be used to compute $C_{p,i}$, allowing for deriving initial guesses to train the surrogate models in Equations (3.1) and (3.2) via least squares regression. For instance, in the case of the first turbine in Equation (3.1), collecting a grid of $n_\lambda\times n_{Re}$ training samples, with n_λ and n_{Re} the number of tip speed ratios and Reynolds numbers in the grid, and enforcing Equation (3.4) in each of the grid points yields a matrix factorization of the form

$$\boldsymbol{C}_{p,1}=\boldsymbol{\Phi}(\boldsymbol{\lambda}_1)\boldsymbol{w}_1\boldsymbol{\Psi}^T(\mathbf{Re}), \tag{3.5}$$

where $\boldsymbol{C}_{p,1}\in\mathbb{R}^{n_\lambda\times n_{Re}}$ is the matrix of power coefficients computed from Equation (3.4) at all training points. The matrix $\boldsymbol{\Phi}(\boldsymbol{\lambda}_1)\in\mathbb{R}^{n_\lambda\times 5}$ is the radial basis function (RBF) matrix evaluated at the tip-speed ratios $\boldsymbol{\lambda}_1$, while $\boldsymbol{\Psi}(\mathbf{Re})\in\mathbb{R}^{n_{Re}\times 3}$ contains the polynomial basis evaluated at the Reynolds numbers $\mathbf{Re}\in\mathbb{R}^{n_{Re}}$. The coefficient matrix $\boldsymbol{w}_1\in\mathbb{R}^{5\times 3}$, with entries $w_{1,m,n}$, contains the parameters to be identified in the surrogate model Equation (3.1) and de facto encodes the performances of the turbine under the dynamical system in Equations (2.2)–(2.3).

These coefficients can be computed by pseudo-inverse on both sides of Equation (3.5):

$$\boldsymbol{w}_{1,0}=\left(\boldsymbol{\Phi}^T\boldsymbol{\Phi}\right)^{-1}\boldsymbol{\Phi}^T\boldsymbol{C}_{p,1}\boldsymbol{\Psi}\left(\boldsymbol{\Psi}^T\boldsymbol{\Psi}\right)^{-1}. \tag{3.6}$$

where $\boldsymbol{w}_{1,0}$ emphasizes that these are the initial guesses for the optimization.

Considering that this estimate acts only as an initial guess, no regularization was used in the least square solution. On the other hand, taking into account the measurement uncertainties was found to improve the initial guess. These were introduced using a classic weighted formulation on the regression of the RBF block, which reads

$$\boldsymbol{w}_{1,0}=\left(\boldsymbol{\Phi}^T\mathbf{N}\boldsymbol{\Phi}\right)^{-1}\boldsymbol{\Phi}^T\mathbf{N}\boldsymbol{C}_{p,1}\boldsymbol{\Psi}\left(\boldsymbol{\Psi}^T\boldsymbol{\Psi}\right)^{-1}, \tag{3.7}$$

where the matrix $\mathbf{N}$ is an estimate of the measurement precision, giving more weight to points with lower uncertainty and defined as

https://doi.org/10.1017/dce.2026.10051 Published online by Cambridge University Press

$$\mathbf{N} = \sigma_{\min}^2 \begin{bmatrix} \frac{1}{\sigma_1^2} & 0 & \dots & 0 \\ 0 & \ddots & 0 & \vdots \\ \vdots & 0 & \ddots & 0 \\ 0 & \dots & 0 & \frac{1}{\sigma_{n_j}^2} \end{bmatrix}, \tag{3.8}$$

where σ_j^2 is the variance of each measurement and $\sigma_{\min} = \min\{\sigma_i\}$. These were used by propagating the measurement uncertainties of u_i, $\tau_{g,i}$ and ω_i through Equation (3.4) using a standard first-order approach. A comparison between weighted and unweighted regressions shows that the inclusion of measurement uncertainties leads to an improvement of approximately 10% in the uncertainty-weighted error (wRMSE), indicating a better agreement with the most reliable data. The solution of the initial set of coefficients from Equation (3.7) can be interpreted as first carry out a weighted least square regression of the model $\mathbf{C_{p,1}} = \mathbf{\Phi A}$, followed by a traditional least square regression of the model $\mathbf{A}^T = \mathbf{\Psi} \boldsymbol{w}_{1,0}^T$.

3.2. Model parameters obtained from a BEM-based model

In order to provide a reference model for comparison, the same parametrization described in Section 3.1 was also constructed using data generated from a classical Blade Element Momentum (BEM) approach. The motivation for introducing a BEM-based model is that it represents the standard tool used in the wind energy community to derive aerodynamic models for control-oriented applications.

In this case, instead of relying on experimental measurements, a grid of operating conditions was generated numerically. In particular, the power coefficient $C_{p,1}$ was evaluated over a set of tip-speed ratios λ_1 and Reynolds numbers Re, forming a synthetic dataset analogous to $\boldsymbol{C}_{p,1}$ in Equation (3.5). The aerodynamic polars of the airfoil, i.e., lift and drag coefficients as a function of the angle of attack, were computed using XFOIL at different Reynolds numbers. These polars were then used within a BEM framework to evaluate the turbine performance, using the `CcBlade` module from the WISDEM Python package (Ning, 2013).

Given this dataset, the same regression framework as in Section 3.1 was employed. In particular, the coefficient matrix was obtained by solving a least squares problem of the form

$$\boldsymbol{C}_{p,1}^{\text{BEM}} = (\boldsymbol{\lambda}_1)\boldsymbol{w}_1^{\text{BEM}\,T}(\mathbf{Re}), \tag{3.9}$$

where $\boldsymbol{C}_{p,1}^{\text{BEM}}$ denotes the matrix of power coefficients obtained from the BEM simulations. The corresponding model coefficients $\boldsymbol{w}_1^{\text{BEM}}$ are computed analogously to Equation (3.6). In this case, no weighting based on measurement uncertainty is introduced, as the dataset is generated numerically.

It is important to note that, although BEM models are widely used and well established for utility-scale wind turbines, their application in the present context must be treated with care. The experiments considered in this work are conducted at a small scale, corresponding to relatively low Reynolds numbers. Under these conditions, the aerodynamic behavior is more difficult to predict accurately, which may result in larger discrepancies. Therefore, the predictions obtained from the BEM-based model in the present study should be interpreted with caution, as they may be significantly less reliable than those usually obtained for conventional full-scale wind turbines.

Finally, it is worth noting that extending the BEM framework to the downstream turbine is not straightforward, due to the presence of wake interactions and the need for an additional wake model. Since this is not the focus of the present study, the BEM-based parametrization is considered here only for the first turbine and is used solely as a reference for comparison purposes.

3.3. A note on local stability

The local stability properties of the steady-state solutions defined by $\tau_{a,i} = \tau_{g,i}$ in Equation (2.3) can be assessed by linearizing the rotor dynamics around a given equilibrium point. Since the control input acts

https://doi.org/10.1017/dce.2026.10051 Published online by Cambridge University Press

on the tip-speed ratio through the rotor speed, the relevant condition is expressed in terms of the local slope of the net torque with respect to λ_i. In open-loop operation, the system generally admits a family of equilibrium points, parameterized by the operating conditions. For a generic turbine i, local asymptotic stability of a given equilibrium requires

$$\frac{\partial f}{\partial \lambda_i} = \frac{1}{J}\left[\frac{1}{2}\rho\pi R^3 u_1^2 \frac{\partial}{\partial \lambda_i}\left(\frac{C_{p,i}}{\lambda_i}\right) - \frac{\partial \tau_{g,i}}{\partial \lambda_i}\right] < 0, \tag{3.10}$$

where the derivative is evaluated with the operating conditions held fixed, namely the freestream velocity u_1 and, for downstream turbines, the upstream tip-speed ratio λ_{i-1}.

It is important to note that, in open-loop operation, not all equilibrium points are necessarily stable. Depending on the operating region, unstable equilibria may also arise. For this reason, stability was not explicitly enforced as a global constraint during identification. Instead, the optimization relies on matching the measured rotor trajectories in the operating regions explored by the data. As a consequence, parameter choices associated with incorrect local stability properties tend to produce trajectories that are inconsistent with the experimental observations, and are therefore penalized by the cost functional. As shown later in the results, this mechanism plays a visible role in the optimization process, where even limited parameter updates may lead to marked changes in the model response once dynamically consistent local behavior is recovered.

3.4. Adjoint-based identification

In this work, the Lagrangian in Equation (2.5) is defined as

$$\mathcal{L}_p(\mathbf{w}_i) = \left(\omega_i^*(t) - \omega_i(t;\mathbf{w}_i)\right)^2. \tag{3.11}$$

The optimization for each turbine is performed independently. This is possible because, in the identification of a downstream turbine, the upstream tip-speed ratio λ_{i-1} is treated as a measured exogenous input. Therefore, the model of turbine i can be identified separately once the corresponding upstream trajectory is provided from the experimental data. The measured time series $\omega_i^*(t)$ is filtered using a 4$^{\text{th}}$ order a Butterworth low-pass filter with a cutoff frequency of $f_{\text{c.o.}} = 2$ Hz chosen based on the turbine's time response to attenuate high-frequency noise.

The cost functions $\mathcal{J}_{w,i}(\mathbf{w}_i)$ are optimized using the Adam optimizer (Kingma and Ba, 2014), preferred over quasi-Newton alternatives such as the BFGS because of its higher robustness to gradient noise. The gradient $\nabla_{\mathbf{w},i}\mathcal{J}_{w,i}$ was computed via an adjoint-based formulation (Sengupta et al., 2014) to avoid solving n_w additional ODEs per evaluation. The adjoint method computes the gradient as

$$\nabla_{\mathbf{w},\mathbf{i}}\mathcal{J}_{w,i}(\mathbf{w}_i) = \int_0^{T_0} s_\lambda^T(t)\left(\frac{\partial f}{\partial \mathbf{w}_i}\right) dt \tag{3.12}$$

where $s_\lambda(t)$ are the adjoint variables. These are obtained by solving the adjoint terminal value problem

$$\begin{cases} \dfrac{ds_\lambda}{dt} = -\left(\dfrac{\partial f}{\partial \omega_i}\right)^\top s_\lambda(t) - \left(\dfrac{\partial \mathcal{L}_p}{\partial \omega_i}\right)^\top, \\ s_\lambda(T_0) = 0 \end{cases} \tag{3.13}$$

where all terms are evaluated at the current guess for the states $\omega_i(t;\mathbf{w}_i)$, which thus requires first a forward integration. We note that the transposition in Equation (3.13) is included for consistency with high dimensional problems but is irrelevant to the problem at hand since both Jacobians are scalars. The adjoint-based evaluation requires one forward pass and one backward pass, regardless of the number of unknown parameters $\mathbf{w}_i$.

Starting from the initialization as in Equation (3.7), the gradient computation is used then to update the weight guess using the ADAM optimizer (Kingma and Ba, 2014)

https://doi.org/10.1017/dce.2026.10051 Published online by Cambridge University Press

$$\mathbf{w}_i^{(n+1)} = \mathbf{w}_i^{(n)} - \eta \frac{\hat{\mathbf{m}}^{(n)}}{\sqrt{\hat{\mathbf{v}}^{(n)}} + \epsilon} \tag{3.14}$$

where n is the iteration number, η is the learning rate, ϵ is a small constant to prevent division by zero, and $\hat{\mathbf{m}}$ and $\hat{\mathbf{v}}$ are filtered momentum parameters computed as follows:

$$\hat{\mathbf{m}}^{(n)} = \frac{\beta_1 \mathbf{m}^{(n-1)} + (1-\beta_1)\nabla_{\mathbf{w},\mathbf{i}} \mathcal{J}_{w,i}^{(n)}}{1-\beta_1^n} \tag{3.15}$$

$$\hat{\mathbf{v}}^{(n)} = \frac{\beta_2 \mathbf{v}^{(n-1)} + (1-\beta_2)\left[\nabla_{\mathbf{w},\mathbf{i}} \mathcal{J}_{w,i}^{(n)}\right]^2}{1-\beta_2^n}, \tag{3.16}$$

where $\mathbf{m}$ and $\mathbf{v}$ are the first and second moment estimates of the gradient, while β_1 and β_2 are the decay rate coefficients for the moments.

Multiple restarts were employed to reset the optimization process whenever a sudden jump in the cost function occurred, typically because the current parameter guess violates the stability condition in Equation (3.10). In such a case, the optimization is restarted to reset the low-pass filtering of the gradient. Additionally, a learning rate schedule was designed to reduce the learning rate once the cost function falls below a predefined threshold. This approach allows the optimizer to take smaller steps and prevent overshooting. It is worth noting that, while uncertainty weighting is introduced in the construction of the initial guess (Section 3.1), it is not explicitly propagated in the adjoint-based dynamic identification. This choice is motivated by the fact that the initial reconstruction of the power coefficient is highly sensitive to measurement noise, particularly due to the cubic dependence on wind speed. In contrast, the dynamic identification relies on the rotor speed signal, which is measured with lower uncertainty, and whose dynamics inherently filter high-frequency fluctuations.

4. Experimental methodology

The detailed experimental setup used to acquire data and interact with the system in real time is described in Section 4.1. The identification methodology is evaluated across multiple scenarios. The first, detailed in Section 4.2, focuses on nonlinear system identification for two turbines operating under low turbulence conditions with varying set points. The second scenario, presented in Section 4.3, simulates a wind farm environment with high turbulence intensity and fixed operating conditions. Finally, the robustness of the identified models is assessed through a control task, as described in Section 4.4.

4.1. Experimental set up

The proposed methodology was experimentally validated using three-bladed wind turbine scale models, originally designed in Coudou et al. (2018). Each model features a rotor diameter of $D = 0.15$ m and a hub height of $z_{\text{hub}} = 0.13$ m. The rotor was designed based on Burton's optimal rotor theory (Sørensen and Sørensen, 2016) and employs a low-Reynolds-number airfoil section (HAM-STD HS1–606). This design enables the turbines to achieve power and thrust coefficient performances comparable to those of full-scale turbines such as the Vestas V66-2 MW offshore turbine, of which it represents a 1:440 scale version. A photograph of the turbines is shown in Figure 2 together with the relevant dimensions and airfoil section. The total moment of inertia of the rotor has been estimated from the CAD model to be $J = 2.5 \times 10^{-6}$ kg m^2.

Each rotor is directly coupled to a DC motor (Faulhaber 1331T006SR) operating as a generator. The blades are fixed, hence the only actuation is through motor torque, adjusted via a variable resistance R_{v} connected to the generator. The generator torque τ_g is modeled electrically by relating it to the current i as $\tau_g = k_\tau \cdot i$ where k_τ is a motor constant. The back electromotive force (EMF) is assumed proportional to the

https://doi.org/10.1017/dce.2026.10051 Published online by Cambridge University Press

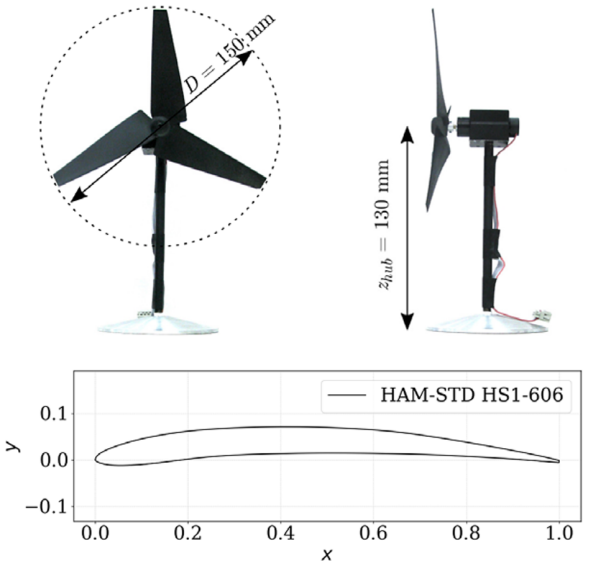


Figure 2. *Wind turbine model used in the experimental campaign (Coudou et al., 2018) and corresponding low-Reynolds-number airfoil used in the blade.*

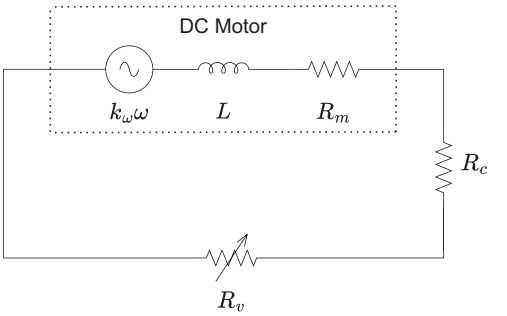


Figure 3. *Electrical model of the wind turbine generator and relevant variables.*

rotor speed: $V_{\text{emf}} = k_\omega \cdot \omega$, with k_ω also a motor-specific constant. Neglecting generator inductance L and applying mesh analysis to the equivalent circuit (Figure 3), the generator torque becomes:

$$\tau_g = k_\tau \cdot \frac{k_\omega \omega}{R_{\text{tot}} + R_{\text{v}}} \tag{4.1}$$

where $R_{\text{tot}} = R_{\text{m}} + R_{\text{c}}$, with R_{m} and R_{c} representing the internal motor and cable resistances, respectively. This relation is used in Equation (2.3) to compute the mechanical torque on the turbine shaft.

The experimental setup with sensors and controllers is illustrated in Figure 4 for the case of two turbines. A Raspberry Pi 4 is employed for real-time data acquisition and turbines' control. Each turbine is equipped with an incremental encoder for measuring the rotational speed $\omega_i^*(t)$. These encoders feature 50 pulses per revolution (PPR), and the rotational speed is computed by an Arduino Nano through the measurement of the time interval between two consecutive pulses.

The free-stream wind speed at hub height $u_1(z_{\text{hub}}, t)$ is measured using a Prandtl tube. The dynamic pressure $\Delta p = \frac{1}{2}\rho u_1^2$, defined as the difference between total p^0 and static pressure p_s, is acquired using an

https://doi.org/10.1017/dce.2026.10051 Published online by Cambridge University Press

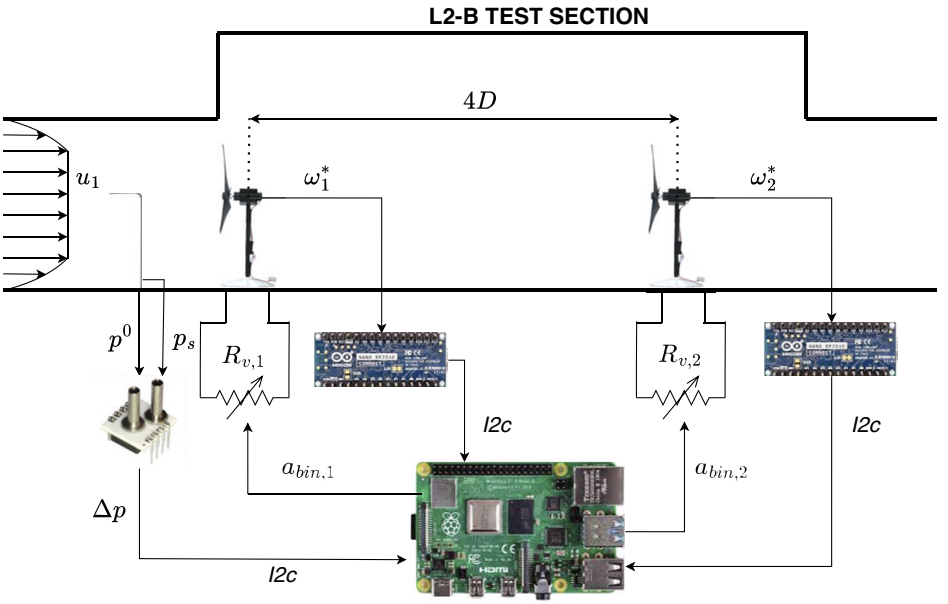


Figure 4. *Experimental setup in the low-turbulence scenario configuration, detailing the measurement of free-stream wind speed u_1, rotational speed ω_i^* of each turbine, and torque actuation via variable resistance $R_{v,i}$ controlled by a 12-bit binary signal $a_{bin,i}$.*

AMS 5812–0000-DB sensor, from which the wind speed is then derived $u_1 = \sqrt{2\Delta p/\rho}$. A thermocouple is installed to monitor air temperature and enhance the accuracy of air density estimations.

Torque actuation is implemented by modulating the electrical load through a bank of 12 resistors, each controlled via MOSFETs. This configuration enables 2^{12} discrete resistance values, ranging from 0.25 Ω to 1024 Ω. A 12-bit binary signal a_{bin} is sent from the Raspberry Pi 4 to a shift register (SNx4HC595), which selects the active resistors. The corresponding resistance R_v is retrieved from a precomputed lookup table.

4.2. Low turbulence scenario identification

The first scenario evaluates the proposed methodology for identifying the aerodynamical characteristics of two wind turbine models in a tandem configuration, where the operational conditions of both turbines are varied (Figure 4). This identification under varying conditions is used for the control implementation, as discussed in Section 4.4. The two wind turbine models are separated by four rotor diameters ($4D \approx 60$ cm). The experimental campaign was conducted in the VKI Wind Engineering facility L2-B, an open-circuit wind tunnel with a test section of dimensions $H = 0.5$m, $W = 0.5$m, and $L = 0.8$m, capable of generating uniform flow velocities up to $U_\infty = 35\text{ms}^{-1}$. The Prandtl tube was positioned approximately two rotor diameters upstream of the first turbine. The limited length of the test section prevents the development of a fully developed boundary layer representative of atmospheric conditions, resulting in low turbulence intensity. The blockage ratio is approximately 5% (Coudou, 2021), which is low enough to avoid significant wake distortion (McTavish et al., 2014).

The system identification process was performed by analyzing the response of $\omega_i^*(t)$ to a combination of control steps in R_v and gradually varying freestream velocities $u_1(t)$. The upstream turbine model was trained using seven episodes, while the downstream turbine model relied on five episodes. Each episode, as described in Section 2, corresponds to a time interval of $T_0 = 32$s, with a data sampling frequency of $f_s = 20$Hz. Both were then tested on four and three unseen wind/loading episodes respectively. The model

https://doi.org/10.1017/dce.2026.10051 Published online by Cambridge University Press

identification for the two turbines was performed in separate episodes: first, the upstream turbine was trained, followed by the downstream turbine, which also utilized data from the first. This approach treats the identification as two distinct processes, even though, in principle, both turbines could be trained jointly. Figure 5 illustrates the input signals used in three training episodes and two testing episodes. The left panel shows the free-stream velocity $u_1(t)$ applied during the training or testing of the upstream turbine ($u_{1,1}(t)$) and during the training or testing of the downstream turbine ($u_{1,2}(t)$). The right panel depicts the corresponding steps in generator resistance for the upstream turbine in the two cases ($R_{1,1}(t)$ and $R_{1,2}(t)$), as well as the generator resistance applied to the downstream turbine during the identification of the waked turbine model ($R_2(t)$).

4.3. High turbulence scenario identification

The second scenario evaluates the proposed methodology in a wind farm configuration consisting of a 3×3 turbine array operating under high turbulence conditions. The experiments were conducted in the VKI Wind Engineering facility L1-B. This is a low-speed, closed-loop wind tunnel with a test section measuring $H = 2\text{m}$, $W = 3\text{m}$, and $L = 20\text{m}$, delivering a maximum wind speed of $U_\infty = 60\text{m/s}$. The length of the test section allows the development of a fully established turbulent boundary layer at the location of the wind farm, which is positioned at the downstream end of the tunnel and thus entirely within the boundary layer. Further details on how the boundary layer generated in the L1-B tunnel replicates atmospheric flow conditions can be found in (Conan, 2012).

A schematic of the experimental setup is shown in Figure 6. The turbine models were arranged with spanwise and streamwise spacings of 3D and 5D, respectively. For the nonlinear identification test, three turbines from the central row of the array were selected: one located in the freestream and two positioned in the wake region. This setup targets turbines operating near their optimal performance point under steady turbulent inflow, consistent with typical wind turbine control strategies. Notably, the freestream wind velocity was not measured directly at the first turbine. Instead, as shown in Figure 6, a Prandtl tube was positioned at a streamwise distance $d_1 = 1.2\,\text{m}$ upstream of the first turbine row, and at a spanwise offset $d_2 = 1\,\text{m}$ from the row centerline. Although the measurement is performed at hub height, it does not provide a rotor-equivalent wind speed representative of the inflow experienced by the turbine, a quantity that is particularly relevant for modeling.

To maintain a consistent operating point, the resistance R_{var} connected to the DC generator was fixed at $R_{\text{val}} = 1\Omega$, corresponding to a tip-speed ratio of $\lambda_1 = 4.5$ for a reference inflow velocity of $u_1 \approx 8.5\text{m/s}$. This value approximately maximizes the power coefficient, as shown in (Coudou, 2021). The experimental setup and measurement procedure matched those described in previous sections. All signals were sampled at $f_s = 20\text{Hz}$ over episodes lasting approximately $T_0 = 20\text{s}$, with 80% of each dataset used for training and the remaining 20% reserved for testing.

4.4. Control under low turbulence conditions

To evaluate the accuracy of the identified models for control purposes, we return to the tandem configuration in Section 4.2. For both turbines, we consider the classic $K\omega^2$ law, commonly used in Region 2 to maximize power extraction (Pao and Johnson, 2009). This controller gives a quadratic torque law

$$\tau_g = K\omega^2, \tag{4.2}$$

where the constant K is defined as (Pao and Johnson, 2009):

$$K = \frac{1}{2}\rho A R^3 \frac{C_{P_{\max}}}{\lambda_{\max}^3}, \tag{4.3}$$

where $\lambda_{\max}$ denotes the tip-speed ratio corresponding to the maximum power coefficient $C_{P_{\max}}$.

https://doi.org/10.1017/dce.2026.10051 Published online by Cambridge University Press

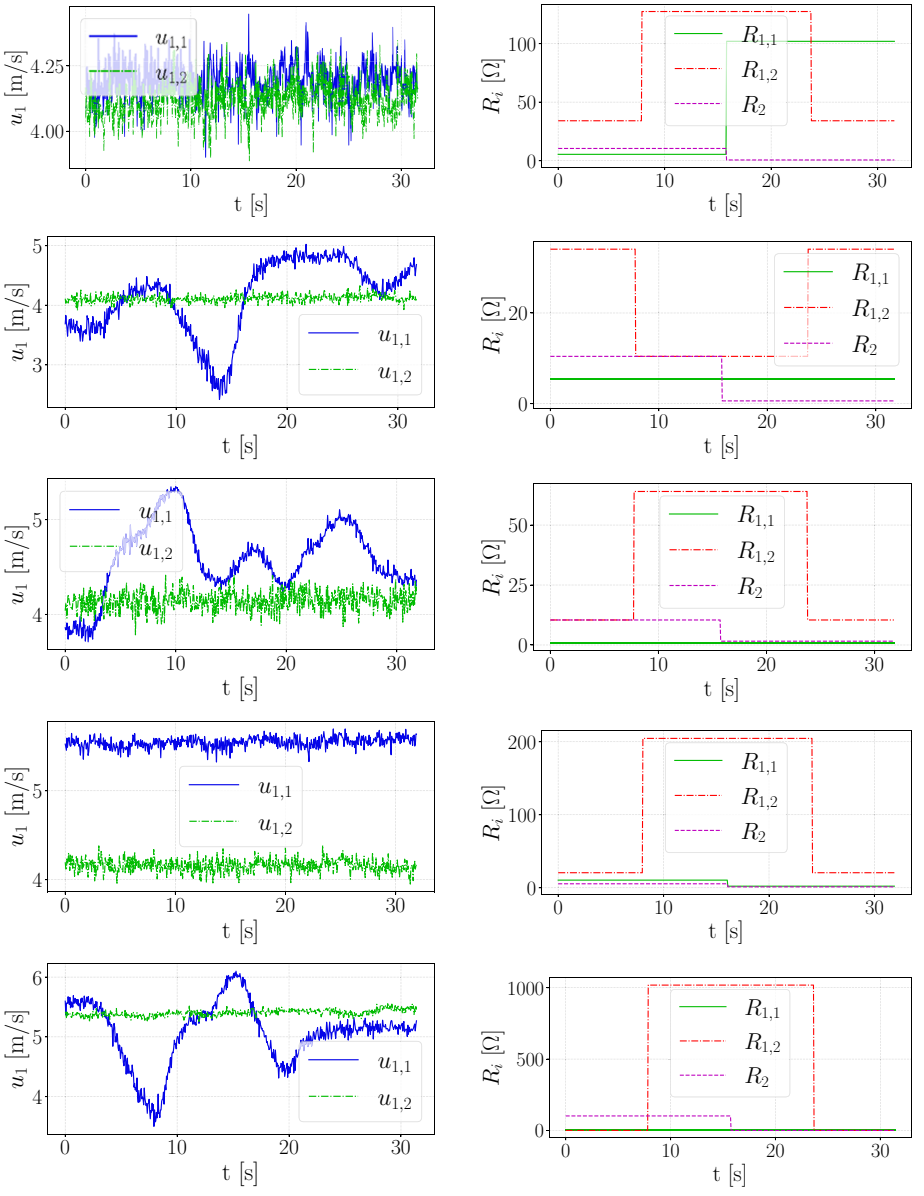


Figure 5. *Free stream velocity (left) and generator resistance evolution (right) for three representative training episodes (first three rows) and two testing episodes for the low turbulence scenario described in Section 4.2.*

In this work, the $K\omega^2$ controller is employed in terms of electrical generator resistance. Combining Equations (4.2) and (4.3) with (4.1) gives

$$R_v = \frac{k_\tau k_\omega}{K\omega} - R_{tot}. \tag{4.4}$$

This model-based control strategy offers a valid test to assess the fidelity of the assimilated dynamic model, as the controller performance is inherently tied to the accuracy of the assumed $C_P(\lambda, Re)$ distribution. Moreover, in the investigated scenario, the controller is not used under typical

https://doi.org/10.1017/dce.2026.10051 Published online by Cambridge University Press

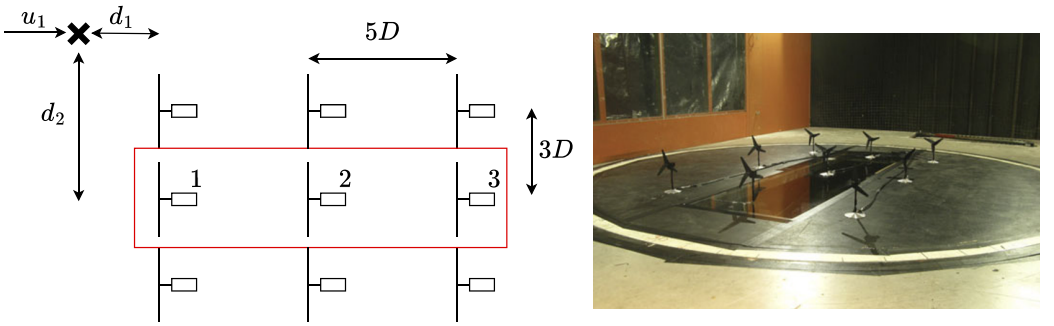


Figure 6. *Wind farm configuration in the VKI Wind Engineering Facility L-1B, with the three identified wind turbines highlighted in red.*

operational assumptions that is to track the tip-speed ratio maximizing power production. Instead, the setpoint in terms of tip-speed ratio is intentionally varied to stress-test the model across a wider operating range.

To ensure reliability of the sensor measurements, all input signals are filtered using a first-order Butterworth low-pass filter with a cutoff frequency of $f_{\text{c.o.}} = 2$ Hz. The performance of the controller is evaluated using three different modeling approaches: (1) the model identified from data, as described in Section 3.4; (2) the parametric model obtained from steady-state data regression through Equation (3.7), which provides the initial guess for the adjoint-based refinement; and (3) the model obtained by regression of Blade Element Momentum (BEM) simulation results, as described by Equation (3.9). This comparison enables an assessment of controller performance under different modeling assumptions.

5. Results

The results are grouped into three subsections. First, Section 5.1 presents the system identification results for the wake tandem configuration in low turbulence conditions described in Section 4.2. Section 5.2 then moves to the identification results in the high turbulence scenario described in Section 4.3. Finally Section 5.3 tests the accuracy of the identified models for model based control purposes.

5.1. Identification in low turbulence

In this scenario, the turbulence fluctuations are small compared to the large-scale variations in the incoming wind velocity. Additionally, the wind velocity is measured at the hub height, consistent with the definitions in Figure 1. As a result, identification is performed under ideal conditions, where the model in Equation (2.3) provides a reliable instantaneous relationship between $\omega_1(t)$ and $u_1(t)$ because these variables are reasonably correlated. This is only true if the torque on the generator of the first turbine remains constant during the episode; otherwise, changes in torque alter the rotational speed independently of the wind speed. Figure 7 shows the time series of these signals, normalized with mean-centering and min-max normalization (scaled quantities denoted with hat) on the left, and a plot showing their strong correlation on the right.

Figure 8 illustrates, on the left, the evolution of the cost function over the optimization iterations for both the upstream (first row) and downstream (second row) wind turbines using all the training episodes. The optimization clearly reduces both cost functions, thus improving the initial guesses from Equation (3.7). Convergence is achieved within a relatively small number of episodes, highlighting the efficiency of the ADAM optimizer with the adjoint-based gradient computation. In the center, Figure 8 shows the power coefficient curves obtained using the initial guesses for the optimization derived from Equation (3.7), based on training grids of $n_{\lambda_1} \times n_{Re}$ and $n_{\lambda_2} \times n_{\lambda_1}$ samples (indicated by red markers) in the

https://doi.org/10.1017/dce.2026.10051 Published online by Cambridge University Press

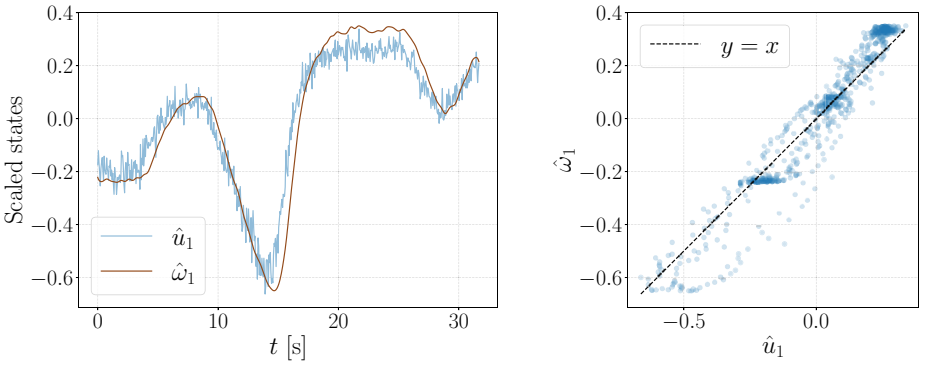


Figure 7. Left: *Time evolution of the hub-height wind velocity of the first turbine ($\hat{u}_1$) and its angular velocity ($\hat{\omega}_1$) for an example test case. Both signals are normalized by mean-centering and min–max scaling.* ***Right:*** *Scatter plot showing the correlation between the two signals. Data are from the "low-turbulence" scenario described in Section 4.2.*

$(\lambda_1 - Re)$ and $(\lambda_2 - \lambda_1)$ planes (as described in Section 3.1). These training samples were selected to cover, as broadly as possible, the physical operating space of both wind turbines.

On the right, Figure 8 presents the final 2D regressions of the power coefficients: for the first turbine (top), as a function of tip-speed ratio and Reynolds number, and for the second turbine (bottom), as a function of the two tip-speed ratios. The scatter points show the states visited in the training dataset (red

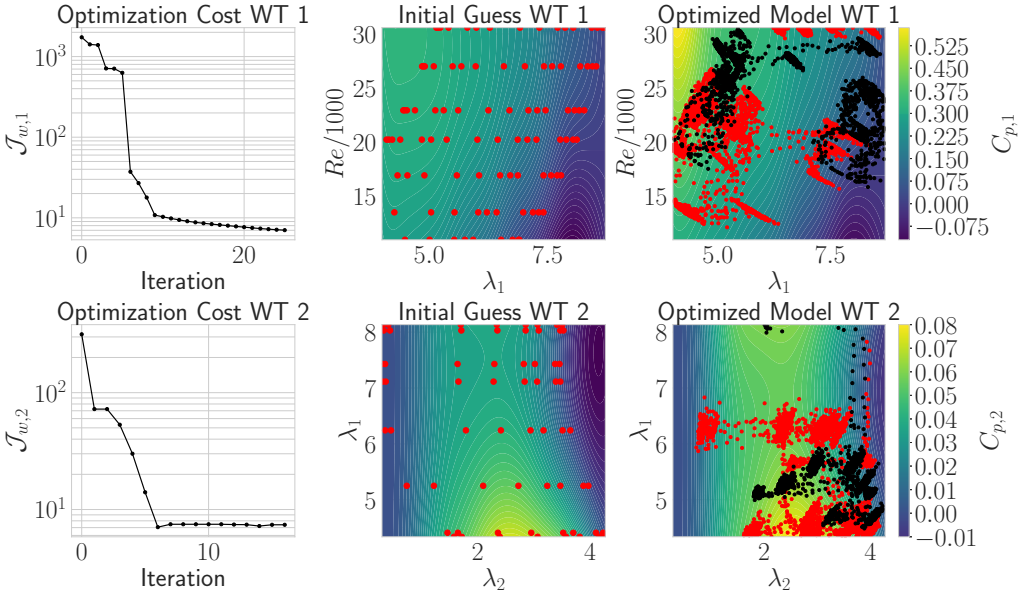


Figure 8. *Evolution of the optimization cost functions (left), initial guesses and training data (center), and optimized models (right) for the power coefficients of the upstream (top row) and downstream (bottom row) wind turbines. The red markers in the center plots represent the steady-state training data points used to obtain the initial guesses for the optimization, whereas in the right plots they correspond to trajectories encountered during the training test cases. Similarly, the black markers represent trajectories encountered during the testing cases.*

https://doi.org/10.1017/dce.2026.10051 Published online by Cambridge University Press

markers) and in the testing dataset (black markers). Overall, these provide good coverage, except in the region of low λ_1 and high Re for the first turbine, and in the regions of (i) high λ_1 and (ii) simultaneously low λ_1 and low λ_2 for the second turbine. For the upstream turbine, this gap in the training data results in a nonphysical model in the unsampled region, highlighting the importance of covering a broad range of operating conditions during training. However, considering that the physical system is unable to reach these conditions (e.g., $\lambda_1 \approx 4$ with $Re \approx 30000$) because of physical limitations, the lack of model accuracy in this area is inconsequential for both predictive and control purposes. For optimization purposes, the model should only be used within the physically admissible operating domain, and the search for the maximum power point should therefore be constrained accordingly. It is worth stressing that the optimized curves do not necessarily reflect the true aerodynamic characteristics of the turbines but rather serve as surrogate models that best reproduce the experimental data, potentially absorbing effects such as measurement noise, generator model errors, or parameter uncertainties (e.g., from CAD estimates).

Figures 9 and 10 show the time evolution of the measured rotational speed of the wind turbines, $\omega_i^*(t)$, represented in black, along with the associated 95% confidence interval (gray shaded area), and the corresponding predictions of the adaptive models. For both the upstream and downstream turbines, we report the model prediction obtained using the optimal solution, shown with a continuous line, and the model prediction using the initial guess for the model coefficients, shown with dashed lines. In addition, for the upstream turbine only, the prediction obtained from the BEM-based model is also reported (blue dash-dotted line). Each figure presents three randomly selected training trajectories and two test trajectories for both turbines, selected from the pool of available training and testing datasets. The adaptive model demonstrates good agreement with the measured trajectories for both turbines, although predictive performances are slightly lower for the waked turbine, particularly in the description of fluctuation at higher frequencies. This can be attributed to two main factors: (1) reduced coherence between the signals at higher frequencies, and (2) the low-pass filtering effect of the identification procedure, which prioritizes the reconstruction of larger-scale variations.

For the upstream turbine, the BEM-based model shows the poorest agreement among the considered models, with larger deviations from the measurements across several test cases. Moreover, the comparison between the initial and optimized models shows that the main improvement lies in a significantly better representation of the system's stability properties. In some cases (Training Cases 2, 3, and Testing Case 2 for the upstream turbine), the initial parameter guess from Equation (3.7) leads the model to be undesirably and unrealistically attracted to the fixed point $\omega = 0$, resulting in shutdown-like behavior that does not match the collected data (see also Section 3.3). On a practical note, we emphasize that the cost function exhibits significant stiffness in regions of the parameter space where changes in stability properties occur. To help the ADAM optimizer adapt to these abrupt changes, we reinitialize it whenever a threshold is crossed ($\Delta \mathcal{J}_{w,i} > 100$), effectively restarting the gradient smoothing procedure in Equation (3.16). This re-initialization occurs, for instance, between iterations 3–4 and 6–7 in the upstream turbine case, as shown in the cost function evolution in Figure 8. Additionally, we observe that once the cost function falls below a small threshold ($\mathcal{J}_{w,i} < 10$), the momentum term becomes detrimental to convergence. In such cases, reducing the learning rate by a factor of 10 improves convergence by enabling finer adjustments in promising regions of the parameter space.

5.2. Identification in high turbulence

As in the previous section, we begin by analyzing the correlation between the normalized incoming velocity $\hat{u}_1(t)$ and the rotational speed of the upstream turbine $\hat{\omega}_1(t)$, shown in Figure 11. This test case corresponds to stationary conditions with high turbulence, where wind speed fluctuates between 7 and 11 m/s. As a consequence that the velocity measurement is not taken at the hub of the turbine, the variables $u_1(t)$ and $\omega_1(t)$ exhibit no meaningful correlation, meaning that it is impossible to reconstruct the turbine's rotational speed time series as done in the previous case. Nonetheless, the objective here is to capture the time-averaged signal, even in the absence of short-term correlation. Although short-term inflow–response

https://doi.org/10.1017/dce.2026.10051 Published online by Cambridge University Press

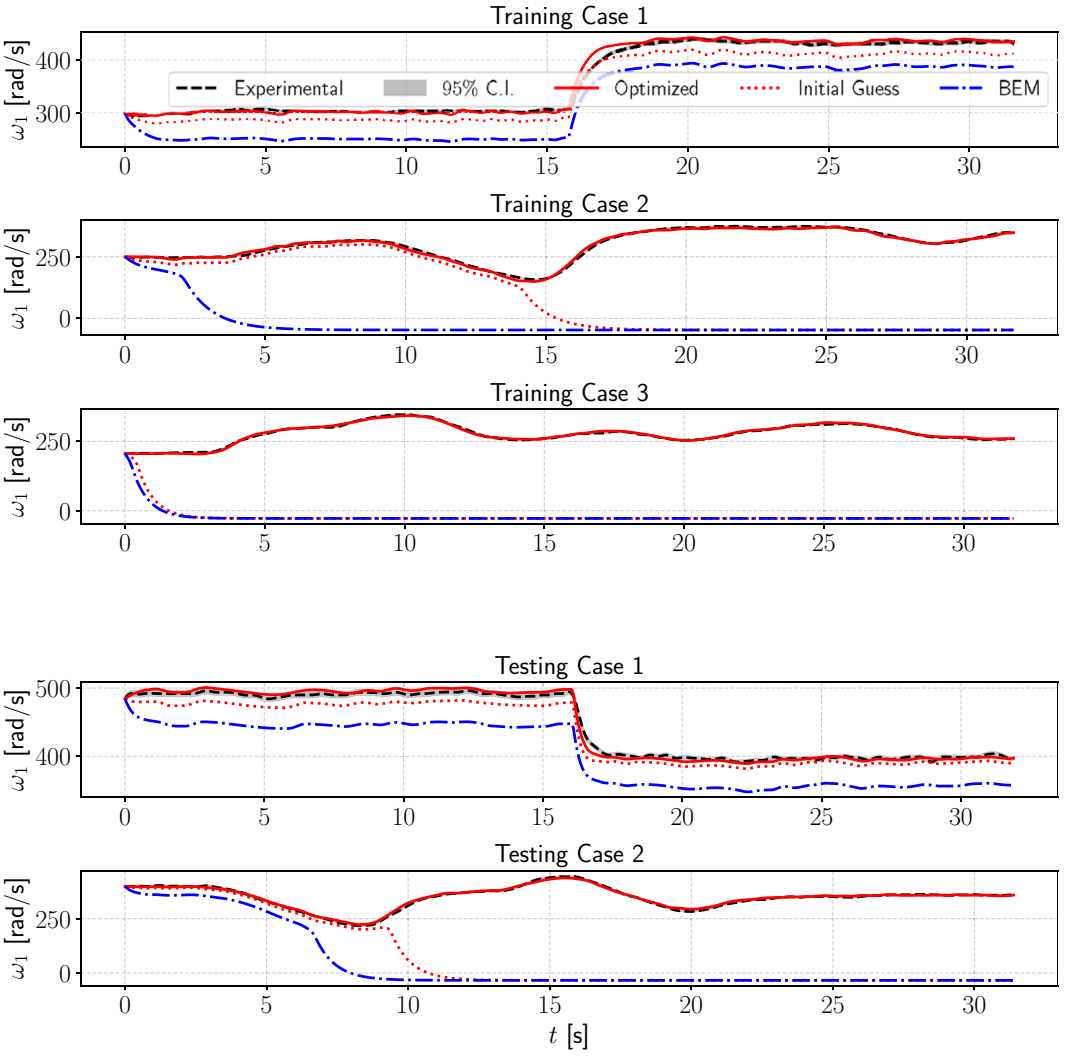


Figure 9. *Time evolution of the measured rotational speed of the upstream wind turbine, $\omega_1^*(t)$ (black line with 95% confidence interval in gray), compared with the predictions from the adaptive models. The solid red line represents the prediction using the optimal solution ($\omega_1(t;\mathbf{w}_1)$), the red dotted line shows the prediction from the initial guess model ($\omega_1(t;\mathbf{w}_{1,0})$), and the blue dash-dotted line corresponds to the prediction obtained from the BEM-based model ($\omega_1\left(t;\boldsymbol{w}_1^{\mathrm{BEM}}\right)$).*

correlation is reduced, the model captures the dominant fluctuations occurring over larger temporal scales, which remain relevant for control-oriented applications.

Figure 12 (top) presents the sampled pairs $Re-\lambda_1$ for the first (upstream) turbine and $\lambda_i-\lambda_{i+1}$ for the downstream (waked) turbines. Samples from the training and test phases are indicated with red and black markers, respectively, while the blue markers represent the states visited by the model when attempting to track the test cases. The orange star indicates the mean value. The dashed line shows the direction of the leading principal component in the sample space.

Two main observations arise. First, although the model does not perfectly reproduce the instantaneous values, the predictions remain well within the distribution of the observed data, with the mean value largely preserved. Second, the correlation in the sample space is significantly higher for the waked

https://doi.org/10.1017/dce.2026.10051 Published online by Cambridge University Press

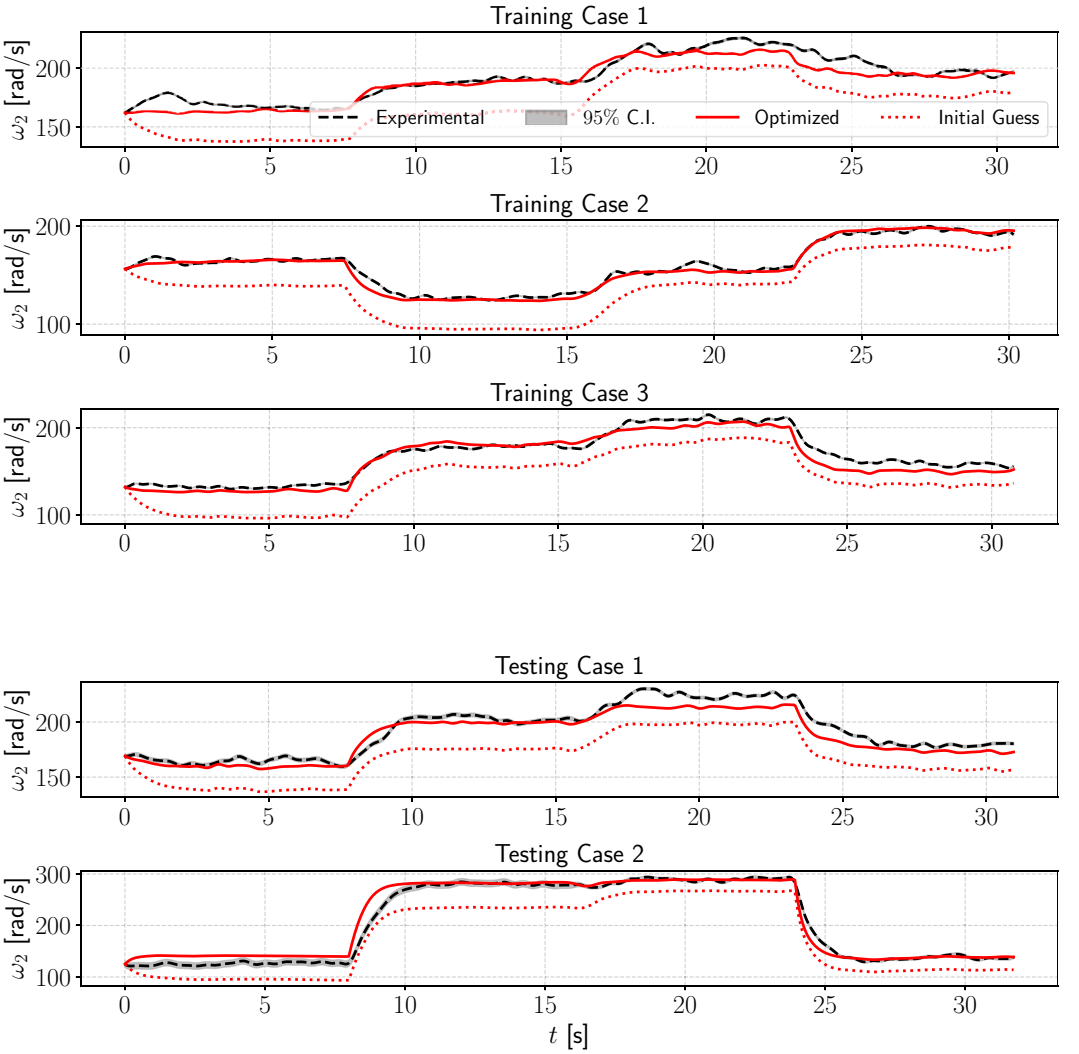


Figure 10. *Time evolution of the measured rotational speed of the downstream wind turbine, $\omega_2^*(t)$ (black line with 95% confidence interval in gray), compared with the predictions from the adaptive models. The solid red line represents the prediction using the optimal solution ($\omega_2(t;\mathbf{w}_2)$), while the red dotted line shows the prediction from the initial guess model ($\omega_2(t;\mathbf{w}_{2,0})$).*

turbines compared to the upstream one. This suggests that, in terms of input/output behavior, the wind farm acts as a low-pass filter on the incoming turbulence.

Figure 12 (bottom) shows the predicted power coefficient along the principal component of the sampled space, comparing the initial guess, the optimized solution obtained from the high-turbulence dataset, and the optimized model previously trained in the low-turbulence scenario and then tested in the present high-turbulence case. In this case, only the physically meaningful range is displayed, as the extrapolated region is associated with non-physical values. The observed discrepancy in performance across the three turbines is expected, as wake effects lead to notably lower power coefficients in the downstream turbines. The substantial difference between the initial and optimized predictions in the high-turbulence case indicates that the optimization significantly modifies the identified model. Its effect is better assessed through comparison with the experimental data discussed later in Figure 13. Of particular

https://doi.org/10.1017/dce.2026.10051 Published online by Cambridge University Press

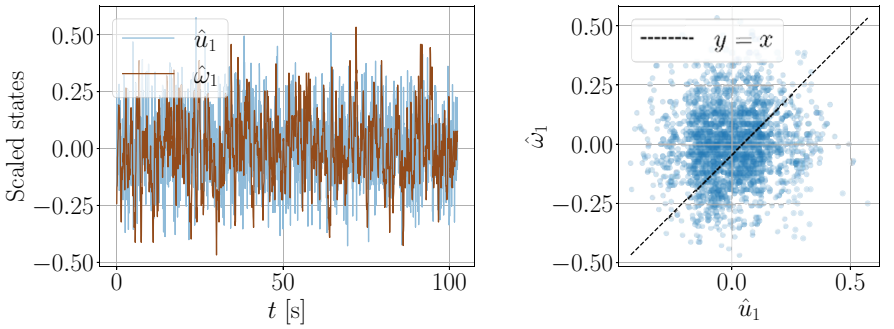


Figure 11. Left: *Time evolution of the dimensionless wind speed at the location highlighted in Figure 6 ($\hat{u}_1$) and the dimensionless rotational speed of the first turbine ($\hat{\omega}_1$).* ***Right:*** *Scatter plot showing the low correlation inflow conditions and turbine dynamics.*

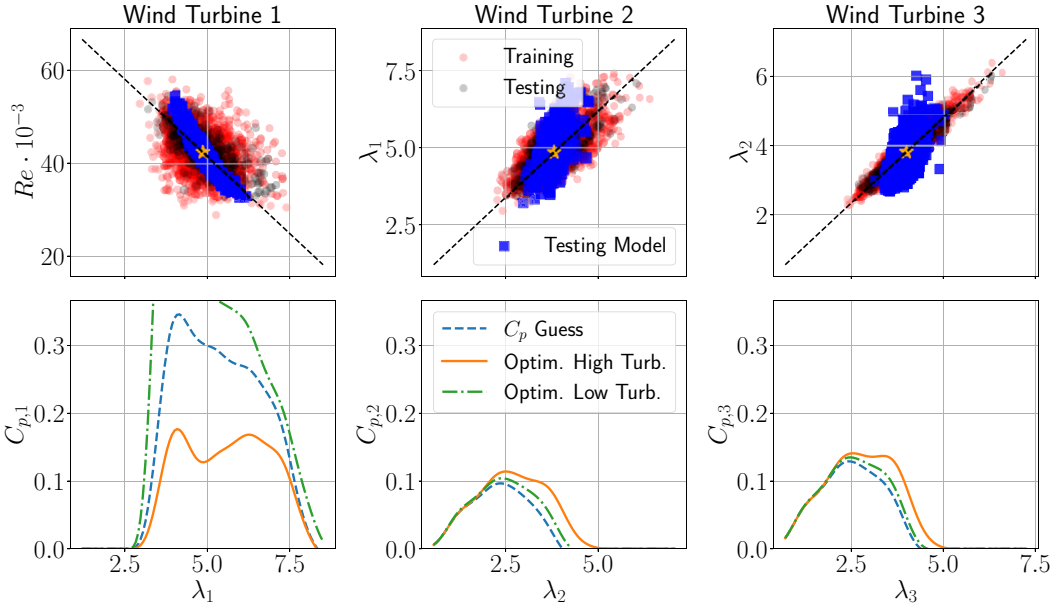


Figure 12. *Summary of the identification result for the wind farm scenario under highly turbulent conditions. The first row shows the location of the sampling and testing points for the three turbines (refer to Figure 6 for their position). The second row shows the power coefficient curves obtained from the initial guess and the optimized weights for the high-turbulence scenario, as well as those corresponding to the low-turbulence scenario. In the bottom-left panel, the low-turbulence optimized model for the first turbine, evaluated under high-turbulence conditions, is displayed only within the physically meaningful range.*

interest is the sensitivity of the upstream turbine's power curve to turbulence intensity: high-frequency fluctuations are filtered out by the turbine dynamics, and thus a model trained in low-turbulence conditions, mainly influenced by large-scale fluctuations, tends to yield overly optimistic and potentially nonphysical predictions. Conversely, for the waked turbines, turbulence enhances wake recovery, although only slightly under these conditions, as the increase in the power coefficient relative to the

https://doi.org/10.1017/dce.2026.10051 Published online by Cambridge University Press

initial guess in the low-turbulence scenario is modest. Consequently, models trained under high-turbulence conditions yield more accurate predictions than those trained in calm flows.

Regarding the shape of the identified power coefficient curves, it is important to consider the sample distribution used for model identification. For example, the apparent double-peaked shape in the upstream turbine's power curve is likely nonphysical and results from insufficient data in the regions $\lambda_1 < 4$ and $\lambda_1 > 6$. However, since these operating conditions are rarely visited, this has little impact on the model's predictive performance. Overall, the strong sensitivity of the identified performance curves to the turbulence conditions in the training data underscores the value of continuously adapting the model over the turbine's operational life. This aligns well with the proposed episodic system identification framework, where the model is not trained once for all but is periodically updated in episodes, each time incorporating newly observed operational data to improve accuracy and robustness.

Finally, Figure 13 shows the model predictions and measured rotational speeds for all three turbines in the test dataset. As in the previous figures, adaptive model predictions are shown as continuous red lines, experimental measurements in black, and the associated uncertainty as a gray confidence band. In addition, red dotted lines show the prediction of the initial guess obtained from Equation (3.7), while for the first turbine only, BEM predictions are shown in dashed-dotted line in blue. The high turbulence environment results in substantial fluctuations in rotational speed across all turbines. For each case, the

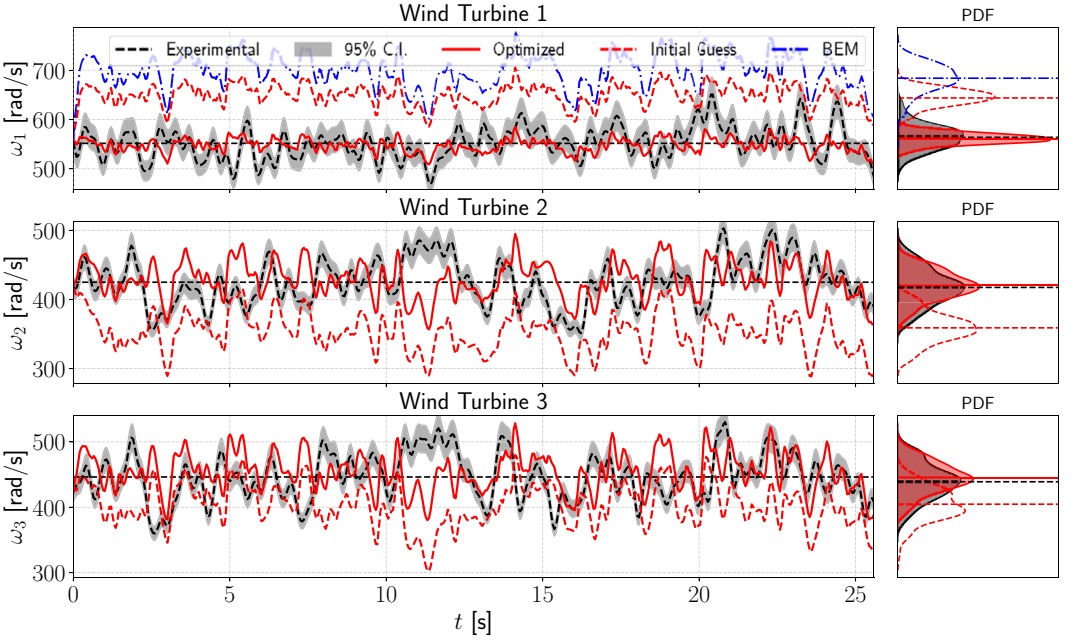


Figure 13. *Model assimilation results for the three wind turbine models under high-turbulence conditions, using the testing dataset. The continuous red lines represent the adaptive model predictions $\omega_i(t;\mathbf{w}_i)$, the black lines correspond to the experimental data $\omega_i^*(t)$, and the gray shaded bands indicate the associated measurement uncertainty (95% confidence interval). The initial-guess predictions are shown as red dotted lines $\omega_i(t;\mathbf{w}_{i,0})$, while the BEM-based predictions for the first turbine are included in blue as dashed-dotted lines $\omega_1\left(t;\boldsymbol{w}_1^{\mathrm{BEM}}\right)$. The plot highlights the substantial fluctuations in rotational speed caused by high turbulence, as well as the inherent limitations of the adaptive model in fully capturing the instantaneous dynamics. Nevertheless, the model successfully reproduces the mean and standard deviation of the waked turbines, whereas the standard deviation of the first turbine is represented with lower accuracy, as evidenced by the probability density function (PDF) distributions shown in the plots on the right.*

https://doi.org/10.1017/dce.2026.10051 Published online by Cambridge University Press

right panel presents the probability density function (PDF) of the measured data and that predicted by the optimized model. In all cases, the mean is accurately captured by the final optimized model, while the standard deviation is slightly underestimated for the upstream turbine, likely due to the weaker input–output correlation in the training data (see Figure 12, top left). By contrast, for the first wind turbine, both the BEM model and the initial-guess model do not accurately capture the mean. However, they provide a better estimate of the standard deviation. This behavior is likely due to the smoother shape of the corresponding power coefficient, whereas the optimized model exhibits this double-peaked structure, which may affect the representation of the variability. Interestingly, the model reconstructs the distributions more accurately for the waked turbines. These results indicate that, under high-turbulence conditions, the model accurately reproduces the statistical behavior of the turbine response, while high-frequency fluctuations are not fully resolved.

5.3. Control performance from identified models

The identified model is integrated in the $K\omega^2$ control law as described in 4.4 for both the upstream and downstream turbine in the low turbulence scenario. The control challenge consists in keeping a reference trajectory in terms of tip-speed ratio, hence define a time varying reference λ (and associated power coefficient) in Equation (4.3) rather than the power maximization. This choice was made to assess the controller performance over a broader portion of the operating domain, instead of restricting the analysis to a single maximum-power operating condition. Such a formulation is also relevant in view of wind-farm control, where the optimal set-point of each turbine may differ from its individual maximum-power point.

The results for the upstream turbine are shown in Figure 14. The top plot displays the dynamic set point alongside the actual tip-speed ratio for three controllers based on different models: (1) the blade element momentum (BEM)-regressed model (green), (2) the initial guess power coefficient curve assuming steady-state conditions (orange), and (3) the adapted model obtained after the identification process

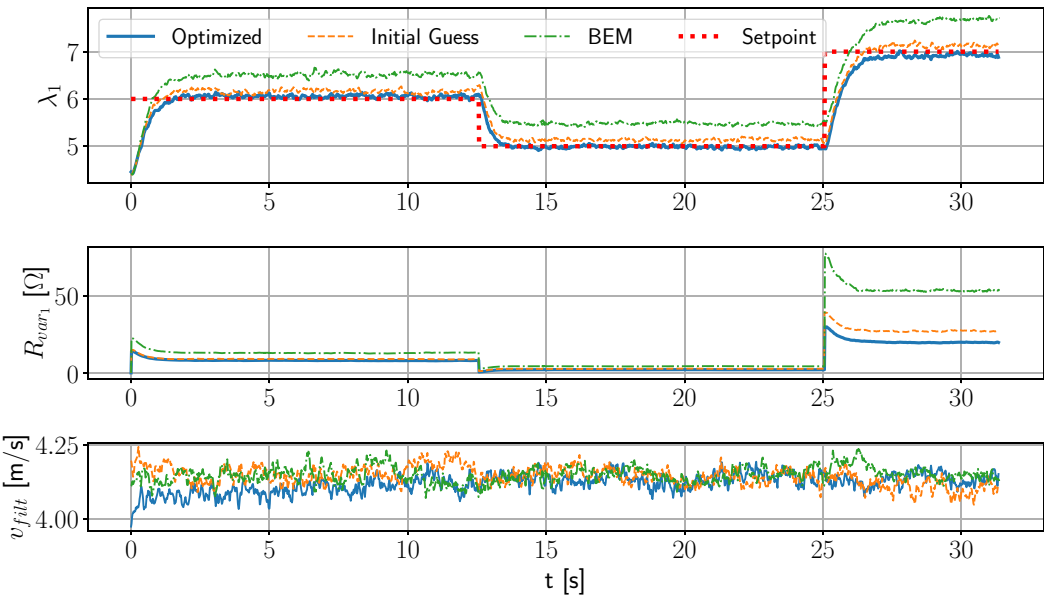


Figure 14. *Test of the adaptive model of the upstream turbine in the low turbulence scenario using the $K\omega^2$ control law. The setpoint in terms of tip speed ratio is highlighted in red. The controller using the adaptive model (blue) is compared with the controller using the model obtained through BEM simulations (green) and steady-state data regression used as an initial guess for the optimization (orange). It can be seen that the controller with the adaptive model outperforms the others.*

https://doi.org/10.1017/dce.2026.10051 Published online by Cambridge University Press

(blue). The middle plot shows the control action, i.e., the variation in generator resistance applied by each controller, while the bottom plot presents the incoming wind velocity during the three control tests, which remained relatively similar. It is worth noting that the large variations in set point were not intended to mimic a realistic control task—which would typically aim to track the optimal power coefficient—but were instead designed to stress-test the controllers.

The superior performance of the controller driven by the adapted model, as compared to the BEM-driven controller, is evident. The large steady-state errors and excessive actuation observed with the BEM-driven controller can be attributed to model deficiencies, which are already apparent from the comparison in Figure 9 and are likely related to the uncertain prediction of low-Reynolds-number effects. Although these could be corrected by more sophisticated control laws, it is interesting to note that the adaptive formulation yields excellent tracking performances with the simplest $K\omega^2$ controller.

The difference in control performances of the initial and adapted model appears minor in comparison. After all, as described in the previous section, the initial guess yields overall satisfactory models as long as the stability properties are preserved. Nevertheless, the difference is appreciable. Considering the impact of power curve modeling on energy production (Pao and Johnson, 2009), and considering that wind turbine dynamics change over their lifespan due to factors such as mechanical wear, environmental conditions, and blade fouling, the ability to adapt and refine the model remains essential for maintaining optimal performance and long-term efficiency.

Finally, a similar analysis is presented for the waked turbine in Figure 15, a scenario well beyond the reach of traditional modeling approaches due to strong inflow unsteadiness and limited flow characterization. Time-dependent set points are prescribed for both turbines. The top plot shows the tracking performance of the upstream turbine, while the second plot presents the response of the downstream turbine, alongside an uncontrolled baseline scenario. The uncontrolled response clearly reveals the wake effect on the second turbine when the upstream set point λ_1 is changed at $t = 25$ s and $t = 50$ s. The third

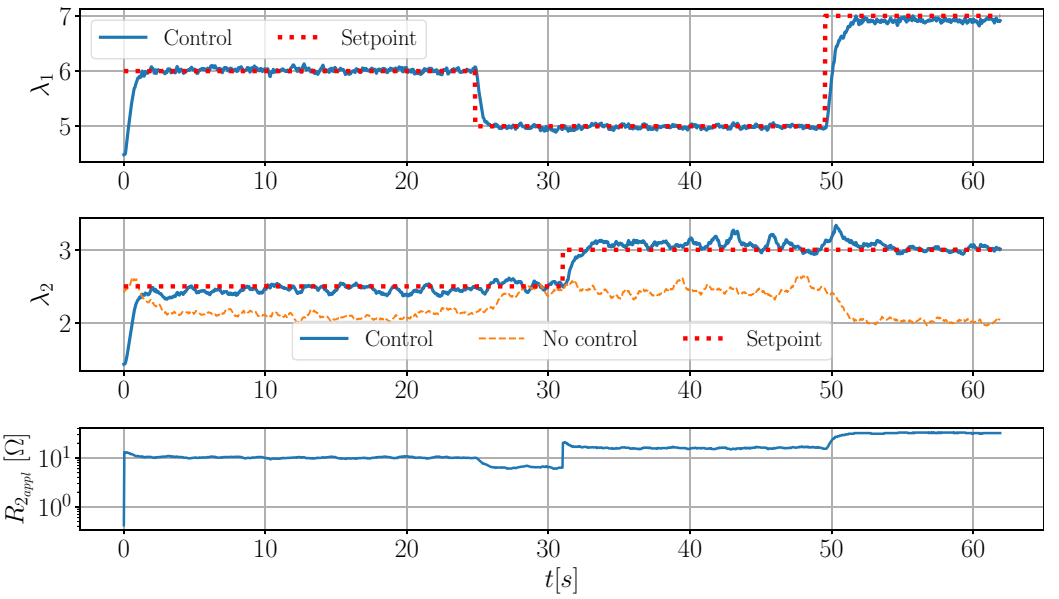


Figure 15. *Test of the adaptive models of the tandem configuration in the low turbulence scenario with the $K\omega^2$ control law. Both the first wind turbine and the downstream turbine are controlled to follow a determined setpoint highlighted in red. A comparison with the uncontrolled case of the downstream turbine (orange) is presented. In this scenario, the effect of the wake is clearly visible, as is the corrective action applied by the controller to the downstream turbine to counteract this effect.*

https://doi.org/10.1017/dce.2026.10051 Published online by Cambridge University Press

plot shows the control input, with a visible actuation step triggered by the set point change, as well as the downstream response to upstream variation.

The key result is highlighted in the second plot: the controller, based on the identified model, successfully mitigates the impact of upstream disturbances (at $t = 25$ s and $t = 50$ s) and accurately tracks the reference step change (at $t = 32$ s). Although some oscillations appear in the controlled λ_2 signal, the overall results demonstrate excellent tracking and disturbance rejection performance within the model bandwidth, even in the presence of wake-induced disturbances. These oscillations can be attributed to an inherent limitation of the $K\omega^2$ controller, which, by design, assumes steady-state operating conditions (see Pao and Johnson, 2009) and lacks feedback control command from the incoming wind velocity. Consequently, its tracking performances degrade under rapidly changing wind conditions because changes in wind velocity are only sensed via changes in rotor speed, which are lagged due to inertia. This limitation is visible for the waked turbine but not for the upstream one, which operates in low turbulence and slow variations of the wind speed.

6. Conclusions

In this work, we proposed and experimentally validated a system identification approach for free-stream and waked wind turbines based on the online estimation of nonlinear power coefficient curves. By combining compactly supported radial basis functions with low-order polynomial regressors, the method yields physically interpretable surrogate representations of turbine performance suitable for control-oriented dynamic models. The methodology was tested on both low- and high-turbulence scenarios using small-scale wind turbines. In the low-turbulence case, the identified models showed strong agreement with the experimental measurements. In the high-turbulence case, although the instantaneous dynamics were not fully reproduced, the models were able to capture the main statistical features of the turbine response despite the unresolved turbulent fluctuations.

The adaptive models were successfully integrated into the $K\omega^2$ controller, demonstrating enhanced performance over conventional control strategies based on BEM or steady-state regressions. In a controlled tandem configuration, the adaptive controllers were able to mitigate wake-induced effects on a downstream turbine, validating the potential of this framework for coordinated wind farm operation. Moreover, the ability of the model to adapt to different operating regimes, including noisy and turbulent conditions, supports its practical applicability. In these conditions, the model captures the statistical and low-frequency behavior of the turbine response, while finer-scale fluctuations remain outside the scope of the present formulation. The proposed identification process, based on adjoint gradient computation and ADAM optimization, enables adaptability while remaining computationally efficient. Importantly, the resulting models retain a structure that is compatible with existing model-based industrial controllers, potentially allowing their integration without major architectural modifications.

Future developments could explore the integration of this adaptive modeling approach into more advanced control strategies such as model predictive control (MPC). At full scale, the proposed framework could use episodic online model updating with the same inputs as the current method: standard SCADA signals and a farm-level freestream velocity estimate, for example from lidar. A practical path is to first identify turbine-specific surrogate power-coefficient models offline to provide an initial guess, then periodically update them during operation to reflect wake interactions, turbulence, and performance degradation from aging or blade surface changes. At the wind-farm level, these updated models could be integrated into existing supervisory or model-based controllers to improve set-point coordination, wake mitigation, and energy capture without redesigning the control architecture.

Despite the promising potential and the implementation pathway outlined above, intermediate steps are still needed before the proposed methodology can be deployed at full scale. This study considers a simplified configuration, with turbines aligned with the incoming flow and operating under controlled inflow. Although the data-driven formulation implicitly captures some unsteady and turbulent effects in the identified power coefficient, additional real wind farm complexities such as yaw misalignment, time-varying wind direction and terrain-induced flow heterogeneity should be included.

https://doi.org/10.1017/dce.2026.10051 Published online by Cambridge University Press

Acknowledgements. The authors gratefully acknowledge the contribution of Jacquet Charles, who worked on the farm testing in the framework of his research master project. The authors also acknowledge the use of AI-based tools to assist in improving the clarity, grammar, and overall readability of the manuscript. All ideas, analyses, results, and scientific content are original and were entirely conceived and developed by the authors.

Data availability statement. The experimental data supporting the findings of this study are openly available in Zenodo (Randino, 2026) at https://doi.org/10.5281/zenodo.19631347.

Author contribution. Conceptualization: S.R. and M.A.M. Methodology: S.R., L.S., N.C., and M.A.M. Investigation: S.R. and M.A.M. Software: S.R. Data curation: S.R. Resources: M.A.M. Writing – original draft: S.R. Writing – review & editing: L.S., N.C., and M.A.M. Supervision: L.S., E.G., and M.A.M. Project administration: M.A.M. Funding acquisition: M.A.M. All authors approved the final submitted draft.

Funding statement. This research was initially developed as part of the research master's project of Sebastiano Randino, supported by a VKI NATO Fellowship. It was subsequently refined and extended during the PhD work of Sebastiano Randino, funded by a FNRS FRIA Fellowship (Fellowship number 40029825). Lorenzo Schena is funded by an FWO Fellowship (number 1567925 N). This work is also part of the RE-TWIST project, which has received funding from the European Research Council (ERC) under the European Union's Horizon Europe programme (grant agreement No 101165479). The views expressed are those of the authors and do not necessarily reflect those of the European Union or the ERC.

Competing interest. The authors declare that they have no known competing financial interests or personal relationships that could have appeared to influence the work reported in this paper.

References

Abbas N, **Zalkind D**, **Pao L and Wright A** (2021) A reference open-source controller for fixed and floating offshore wind turbines. *Wind Energy Science Discussions 2021*, 1–33.

Abdullah MA, **Yatim AHM**, **Tan CW and Saidur R** (2012) A review of maximum power point tracking algorithms for wind energy systems. *Renewable and Sustainable Energy Reviews 16*(5), 3220–3227. https://doi.org/10.1016/j.rser.2012.02.016.

Allen MS, **Sracic MW**, **Chauhan S and Hansen MH** (2011) Output-only modal analysis of linear time-periodic systems with application to wind turbine simulation data. *Mechanical Systems and Signal Processing 25*(4), 1174–1191.

Annoni J, **Howard KB**, **Seiler PJ and Guala M** (2015) System identification of a wind turbine Array. In *33rd Wind Energy Symposium*. Reston, VA, USA: American Institute of Aeronautics and Astronautics (AIAA), AIAA 2015-0221. https://doi.org/10.2514/6.2015-0221

Asghar AB and Liu X (2017) Estimation of wind turbine power coefficient by adaptive neuro-fuzzy methodology. *Neurocomputing 238*, 227–233.

Aslipour Z and Yazdizadeh A (2019) Identification of nonlinear systems using adaptive variable-order fractional neural networks (case study: A wind turbine with practical results). *Engineering Applications of Artificial Intelligence 85*, 462–473.

Bastankhah M and Porté-Agel F (2017) A new miniature wind turbine for wind tunnel experiments. Part I: Design and performance. *Energies 10*(7), 908.

Bharani R and Sivaprakasam A (2022) Application of fuzzy logic method in wind turbine yaw control system to obtain maximum energy: A methodological and prototype approach. *Electrical Engineering 104*, 1373–1387. https://doi.org/10.1007/s00202-021-01396-1.

Bhatt AH, **Bernardoni F**, **Leonardi S and Zare A** (2022) Stochastic dynamical wake modeling for wind farms. Preprint, arXiv: 2208.12196.

Borunda M, **Garduno R**, **de la CSJ and Díaz RAF** (2024) Intelligent control of an experimental small-scale wind turbine. *Energies 17*(22), 1–32.

Bossanyi E, **Savini B**, **Iribas M**, **Hau M**, **Fischer B**, **Schlipf D**, **van Engelen T**, **Rossetti M and Carcangiu C** (2012) Advanced controller research for multi-MW wind turbines in the UPWIND project. *Wind Energy 15*(1), 119–145.

Caduff M, **Huijbregts MA**, **Althaus HJ**, **Koehler A and Hellweg S** (2012) Wind power electricity: The bigger the turbine, the greener the electricity? *Environmental Science & Technology 46*(9), 4725–4733.

Campobasso MS, **Castorrini A**, **Ortolani A and Minisci E** (2023) Probabilistic analysis of wind turbine performance degradation due to blade erosion accounting for uncertainty of damage geometry. *Renewable and Sustainable Energy Reviews 178*, 113254.

Cao K, **Shaler K and Johnson N** (2022) Comparing wind turbine aeroelastic response predictions for turbines with increasingly flexible blades. In *Journal of Physics: Conference Series 2265*. 3, 032025.

Castillo OC, **Andrade VR**, **Rivas JJR and González RO** (2023) Comparison of power coefficients in wind turbines considering the tip speed ratio and blade pitch angle. *Energies 16*(6), 2774.

Chatterjee J and Dethlefs N (2021) Scientometric review of artificial intelligence for operations & maintenance of wind turbines: The past, present and future. *Renewable and Sustainable Energy Reviews 144*, 111051. https://doi.org/10.1016/j.rser.2021.111051.

Chhipa AA, **Kumar V**, **Joshi RR**, **Chakrabarti P**, **Jasinski M**, **Burgio A**, **Leonowicz Z**, **Jasinska E**, **Soni R and Chakrabarti T** (2021) Adaptive neuro-fuzzy inference system-based maximum power tracking controller for variable speed WECS. *Energies 14*(19), 6275.

Conan B (2012) *Wind Resource Accessment in Complex Terrain by Wind Tunnel Modelling. PhD Dissertation*, Université d'Orléans.

Coudou N (2021) Numerical and experimental investigations of the meandering phenomenon in wind turbine wakes. PhD dissertation, UCL-Université Catholique de Louvain.

Coudou N, **Buckingham S**, **Bricteux L and Beeck J** van (2018) Experimental study on the wake meandering within a scale model wind farm subject to a wind-tunnel flow simulating an atmospheric boundary layer. *Boundary-Layer Meteorology 167*, 77–98.

Echiheb F, **Ihedrane Y**, **Bossoufi B**, **Bouderbala M**, **Motahhir S**, **Masud M**, **Aljahdali S and ElGhamrasni M** (2022) Robust sliding-backstepping mode control of a wind system based on the DFIG generator. *Scientific Reports 12*, 11782. https://doi.org/10.1038/s41598-022-15960-7.

Gebel J, **Rezaei A**, **Vemuri A**, **Liverud Krathe V**, **Daems PJ**, **Matthys JJ**, **Sterckx J**, **Vratsinis K**, **Kestel K**, **Nejad AR and Helsen J** (2025) System identification of offshore wind turbines for model updating and validation using field measurements. *Wind Energy Science Discussions*. https://doi.org/10.5194/wes-2024-173.

Gros S and Schild A (2017) Real-time economic nonlinear model predictive control for wind turbine control. *International Journal of Control 90*(12), 2799–2812.

Gu S, **Yang L**, **Du Y**, **Chen G**, **Walter F**, **Wang J and Knoll A** (2024) *A review of safe reinforcement learning: methods, theory and applications.* Preprint, arXiv:2205.10330 [cs.AI] .

Guediri A, **Hettiri M and Guediri A** (2023) Modeling of a wind power system using the genetic algorithm based on a doubly fed induction generator for the supply of power to the electrical grid. *PRO 11*(3), 952.

Hosseinpour AH, **Khosravi MA and Khaloozadeh H** (2017) Improving maximum power point tracking of a wind turbine using power coefficient estimation. In *2017 Iranian Conference on Electrical Engineering (ICEE)*. Piscataway, NJ, USA: IEEE, pp. 697–702.

Houtzager I, **Kulscar B**, **van Wingerden JW van and Verhaegen M** (2010) System identification for the control of wind turbine systems. In *Proc. 3rd Conf. Sci. Making Torque Wind*, 1–10.

Jasniewicz B and Geyler M (2011) Wind turbine modelling and identification for control system applications. In *Scientific Proceedings of the EWEA 2011*. Brussels, Belgium: European Wind Energy Association (EWEA), pp. 280–284.

Jelavic M, **Perc N and Petrovic I** (2006) Identification of wind turbine model for controller design. In *2006 12th International Power Electronics and Motion Control Conference*. Piscataway, NJ, USA: IEEE, pp. 1608–1613.

Kelouwani S and Agbossou K (2004) Nonlinear model identification of wind turbine with a neural network. *IEEE Transactions on Energy Conversion 19*(3), 607–612.

Khurshid A, **Mughal MA**, **Othman A**, **Al-Hadhrami T**, **Kumar H**, **Khurshid I**, **Arshad and Ahmad J** (2022) Optimal pitch angle controller for DFIG-based wind turbine system using computational optimization techniques. *Electronics 11*(8), 1290.

Kingma DP and Ba J (2014) *Adam: A method for stochastic optimization. Preprint, arXiv:1412.6980.*

Kumar A and Stol K (2010) Simulating feedback linearization control of wind turbines using high-order models. *Wind Energy 13*(5), 419–432.

Laks JH, **Pao LY and Wright AD** (2009) Control of wind turbines: Past, present, and future. In *2009 American Control Conference*. IEEE, pp. 2096–2103.

Leishman JG (2002) Challenges in modeling the unsteady aerodynamics of wind turbines. *Wind Energy Symposium. 7476*, 141–167.

Maafa A, **Mellah H**, **Benaouicha K**, **Babes B**, **Yahiou A and Sahraoui H** (2024) Fuzzy logic-based smart control of wind energy conversion system using cascaded doubly fed induction generator. *Sustainability 16*(21), 9333. https://doi.org/10.3390/su16219333.

Mahmoud MS and Qureshi A (2012) Model identification and analysis of small-power wind turbines. *International Journal of Modelling, Identification and Control 17*(1), 19–31.

Majout B, **Bossoufi B**, **Karim M**, **Skruch P**, **Mobayen S**, **El Mourabit Y and Laggoun ZEZ** (2024) Artificial neural networkbased direct power control to enhance the performance of a PMSG-wind energy conversion system under real wind speed and parameter uncertainties: An experimental validation. *Energy Reports 11*, 4356–4378.

Marques PA, **Ahizi S and Mendez MA** (2024) Real-time data assimilation for the thermodynamic modeling of cryogenic storage tanks. *Energy 302*, 131739. https://doi.org/10.1016/j.energy.2024.131739.

McTavish S, **Feszty D and Nitzsche F** (2014) An experimental and computational assessment of blockage effects on wind turbine wake development. *Wind Energy 17*(10), 1515–1529.

Monroy A and Alvarez-Icaza L (2006) Real-time identification of wind turbine rotor power coefficient. In *Proceedings of the 45th IEEE Conference on Decision and Control*. Piscataway, NJ, USA: IEEE, pp. 3690–3695.

Nelles O (2020) *Nonlinear Dynamic System Identification*. Cham, Switzerland: Springer.

Ning SA (2013) tech. rep. CCBlade. National Renewable Energy Laboratory (NREL), Golden, CO (United States).

Pande J and Nasikkar P (2023)A Maximum power point tracking technique for aWind power system based on the trapezoidal rule. *Energies 16*(6), 2799. https://doi.org/10.3390/en16062799.

Pao LY and Johnson KE (2009) A tutorial on the dynamics and control of wind turbines and wind farms. In *2009 American Control Conference*. IEEE, pp. 2076–2089.

https://doi.org/10.1017/dce.2026.10051 Published online by Cambridge University Press

Papi F, **Jonkman J**, **Robertson A and Bianchini A** (2023) Going beyond BEM with BEM: An insight into dynamic inflow effects on floating wind turbines. *Wind Energy Science Discussions*, Under review. https://doi.org/10.5194/wes-2023-57.

Petković D, **Ćojbašič Ž and Nikolić V** (2013) Adaptive neuro-fuzzy approach for wind turbine power coefficient estimation. *Renewable and Sustainable Energy Reviews 28*, 191–195.

Porté-Agel F, **Bastankhah M and Shamsoddin S** (2020) Wind-turbine and wind-farm flows: A review. *Boundary-Layer Meteorology 174*(1), 1–59.

Pusch M, **Stockhouse D**, **Abbas N**, **Phadnis M and Pao L** (2024) Optimal operating points for wind turbine control and co-design. *Wind Energy 27*(11), 1286–1301.

Rai S, **Yang SY and Tsao TC** (2017) Wind turbine system identification and individual pitch control. In *American Control Conference (ACC)*, Vol. *2017*. Piscataway, NJ, USA: IEEE, pp. 1371–1376.

Randino S (2026) *[dataset] Nonlinear system identification for model-based control of waked wind turbines – Experimental data.* https://doi.org/10.5281/zenodo.19631347.

Ribeiro AF, **Casalino D and Ferreira CS** (2023) Nonlinear inviscid aerodynamics of a wind turbine rotor in surge, sway, and yaw motions using a free-wake panel method. *Wind Energy Science 8*(4), 661–675.

Saint-Drenan YM, **Besseau R**, **Jansen M**, **Staffell I**, **Troccoli A**, **Dubus L**, **Schmidt J**, **Gruber K**, **Simões SG and Heier S** (2020) A parametric model for wind turbine power curves incorporating environmental conditions. *Renewable Energy 157*, 754–768.

Schena L, **Gillyns E**, **Munters W**, **Buckingham S and Mendez MA** (2022) Wind turbine control using machine learning techniques. In *ECCOMAS Congress 2022-8th European Congress on Computational Methods in Applied Sciences and Engineering*, pp. 1–10

Schena L, **Marques P**, **Poletti R**, **Ahizi S**, **Berghe JVd and Mendez MA** (2023) *Reinforcement Twinning: from digital twins to model-based reinforcement learning. Preprint, arXiv:2311.03628.*

Schlipf D, **Schlipf DJ and Kühn M** (2013) Nonlinear model predictive control of wind turbines using LIDAR. *Wind Energy 16*(7), 1107–1129.

Sengupta B, **Friston KJ and Penny WD** (2014) Efficient gradient computation for dynamical models. *NeuroImage 98*, 521–527.

Shapiro CR, **Gayme DF and Meneveau C** (2021) Turbulence and control ofWind farms. *Annual Review of Control, Robotics, and Autonomous Systems 4*, 349–372. https://doi.org/10.1146/annurev-control-061820-083849.

Sierra-García JE and Santos M (2020) Exploring reward strategies for wind turbine pitch control by reinforcement learning. *Applied Sciences 10*(21), 7462.

Silva JG, **Ferrari R and Wingerden JW** van (2022) Convex model predictive control for down-regulation strategies in wind turbines. *arXiv preprint.* arXiv: 2209.11087[eess.SY] . https://arxiv.org/abs/2209.11087.

Simani S (2012) Application of a data-driven fuzzy control design to a wind turbine benchmark model. *Advances in Fuzzy Systems 2012*(1), 504368.

Simani S and Castaldi P (2013) Data-driven and adaptive control applications to a wind turbine benchmark model. *Control Engineering Practice 21*(12), 1678–1693.

Sindareh Esfahani P and Pieper JK (2021) Machine learning based model linearization of a wind turbine for power regulation. *International Journal of Green Energy 18*(15), 1565–1583.

Soler D, **Mariño O**, **Huergo D**, **de FM and Ferrer E** (2024) Reinforcement learning to maximize wind turbine energy generation. *Expert Systems with Applications 249*, 123502.

Son G, **Lee HJL and Park JW** (2009) Estimation of wind turbine rotor power coefficient using RMP model. *IEEE Industry Applications Society Annual Meeting. IEEE 2009*, 1–8.

Sørensen JN and Sørensen JN (2016) Optimum Rotor Performance Based on Momentum Theory. *General Momentum Theory for Horizontal Axis Wind Turbines*. Cham, Switzerland: Springer, pp. 59–74.

Staffell I and Green R (2014) How does wind farm performance decline with age? *Renewable Energy 66*, 775–786.

Tomin N, **Kurbatsky V and Guliyev H** (2019) Intelligent control of a wind turbine based on reinforcement learning. In *2019 16th Conference on Electrical Machines, Drives and Power Systems (ELMA)*. Piscataway, NJ, USA: IEEE, pp. 1–10.

Verwaal N, **Van Der Veen G and Van Wingerden J** (2015) Predictive control of an experimental wind turbine using preview wind speed measurements. *Wind Energy 18*(3), 385–398.

WindEurope (2015) *Wind in Power: 2014 European Statistics.* Accessed: 2025-04-10. Available at https://www.ewea.org.

WindEurope (2025) Wind energy in Europe – 2024 statistics and the outlook for 2025–2030. Brussels. Available at https://windeurope.org (accessed April 10, 2025).

Wright AD and Fingersh LJ (2008) Tech. Rep. Advanced control design for wind turbines; part I: Control design, implementation, and initial tests. National Renewable Energy lab.(NREL), Golden, CO (United States).

Yap B, **Dodson L and Busawon K** (2012) Online estimation of the power coefficient in wind energy conversion systems. In *2nd International Symposium on Environment Friendly Energies and Applications*, Vol. *2012*. Piscataway, NJ, USA: IEEE, pp. 458–463.

Zribi M, **Alrifai M and Rayan M** (2017) Sliding mode control of a variable-speed wind energy conversion system using a squirrel cage induction generator. *Energies 10*(5), 604. https://doi.org/10.3390/en10050604.

Cite this article: Randino S, Schena L, Coudou N, Garone E and Mendez MA (2026). Nonlinear system identification for model-based control of waked wind turbines. *Data-Centric Engineering*, 7, e18. doi:10.1017/dce.2026.10051

https://doi.org/10.1017/dce.2026.10051 Published online by Cambridge University Press